UNIVERSITÀ DEGLI STUDI DI PADOVA

Department of Industrial Engineering

Master's Degree in Aerospace Engineering

Direct numerical simulation of a hypersonic turbulent boundary layer in realistic conditions

---

Advisor:

Prof. Francesco Picano

Co-advisor:

Ing. Michele Cogo

Candidate:

Anna Grandi

2022549

Anno Accademico 2022/2023

Contents

1 Sommario

I sistemi di protezione termica (TPS), tipici dei flussi supersonici e ipersonici,agiscono sulla superficie dei veicoli ad alta velocità come elementi distribuiti di rugosità, che causano un aumento di resistenza e trasferimento di calore. Esistono pochi studi sperimentali e numerici su flussi ipersonici con rugosità. la tecnica computazionale principale sono le simulazioni numeriche dirette (DNS).
Sono state effettuate tre simulazioni numeriche dirette (DNS) di un flusso ipersonico su una lastra piana.
Le simulazioni riproducono una delle tipologie di roughness dell'esperimento svolto da Williams et al. [19]: due simulazioni con una serie di barrette di sezione quadrata, le cui dimensioni caratteristiche sono una la metà dell'altra, e una simulazione su lastra piana con superficie liscia. Vengono poi analizzate le componenti normale e parallela a parete del flusso per le variabili densità, velocità, temperatura e numero di Mach, le statistiche medie di temperatura, velocità e spessore strato limite, e le radici medie quadratiche delle fluttuazioni di velocità e temperatura. I risultati dei due studi (sperimentale e numerico) sono stati comparati e risultano essere consistenti.

2 Abstract

Thermal Protection Systems (TPS), typical of supersonic and hypersonic flows, acts on the surface of high-speed vehicles as distributed roughness elements, which cause an increase in drag and heat transfer. There are very few experimental and numerical studies on hypersonic flow over roughness. The main computational technique is Direct Numerical Simulation (DNS).
Three Direct Numerical Simulations (DNS) of an hypersonic flow over a flat plate were performed.
The simulations reproduce one of the roughness conditions of the experiment performed by Williams et al. [19]: two simulations with a series of square bars elements, whose characteristic dimensions are one the half of the other, and one simulation over a flat plate with smooth surface. Follows the analysis of the wall- normal and wall-parallel components of the flow for density, velocity, temperature and Mach number, the averaged statistics of temperature, velocity and boundary layer thickness, and the root mean square statistics of velocity and temperature fluctuations. The results of the two studies (experimental and numerical) have been compared and they turned out to be consistent.

3 Introduction

Several aspects of our life are strongly dependent on services that operate thanks to satellites, such as GPS, telephone services, broadband internet, climate and environmental monitoring, search and rescue. For this reason, the possibility to go into space is a matter of great importance.
The study of turbulent flows over a flat plane is one key problem in the design of high speed vehicles; an important example of such vehicles is the re-entry of space launchers from space. Due to the high operational costs involved in space exploration, the goal would be to achieve the reusability of space launchers, that are now only partially reusable because, to escape Earth's gravity, space missions rely on multistage rockets. The main problem is the fact that capsules during reentry have to resist multiple cycles of thermal loads, and this leads to the importance of the thermal protection system (TPS), various materials applied externally to the outer structural skin on an orbiter to maintain acceptable temperatures, which have to be reliable in order to protect the vehicle from the system failure and also the crew, in the case of manned space missions [17].
There are two types of TPS, ablative or tiled. The first is a semi-passive TPS that involves heat absorption through the loss of material. There are some types of plastics reinforced with organic fibers that when exposed to a high-temperature environment undergo pyrolysis. This process generates hot gasses that take away the heat from the layer by blowing the boundary layer away from the surface. The surface ablates with a nonuniform recession rate, resulting in regular [18] [13] or irregular [7] distributed roughness patterns, depending on the type of material. Because of its method of operation, this type of TPS is not reusable. The tiled type, on the other hand, is reusable. It consists in a series of ceramic or carbon tiles that can have a square, diamond or hexagonal shape, and the presence of space between the tiles is what forms a structured roughness pattern on the surface. Another example of compressible flows over roughness is found in transonic turbines, where the blades are subjected to erosion, forming irregular surface patterns, or at the wing leading edge of an aircraft due to icing.

All this brings to the necessity to know more about the effect that such types of roughness geometries have on the flow in order to optimize the design of the thermal protection systems of high speed vehicles like the ones previously mentioned.

Figure 1: Tiled thermal protection systems on the Space Shuttle spacecraft

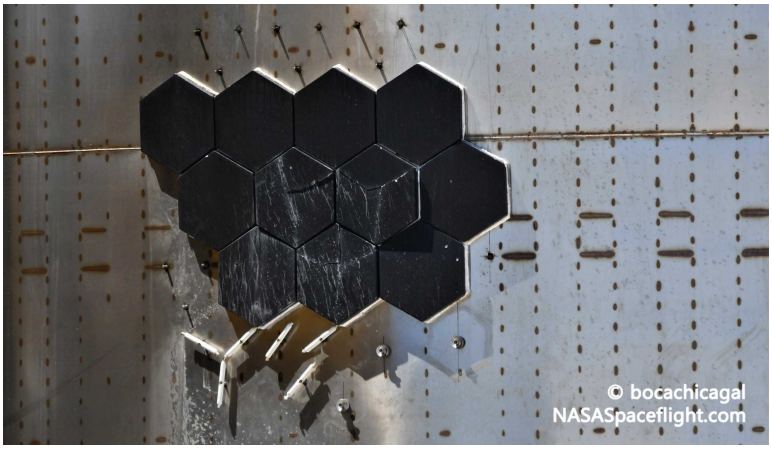

Figure 2: Tiled thermal protection systems on the SpaceX spacecraft

The state of the art of the research on turbulent boundary layer of incompressible flows is still at his early stages; despite the fact that compressible flows over rough surfaces is an important subject in various fields of study, most of the studies on rough walls are limited to the incompressible flow regime, which is well documented both from the experimental and numerical (the most recent are Jiménez 2004 [6], Flack Schultz 2014 [4], [20], Chung 2021 [2]). Incompressible flows have been deeply studied for several years, and these works produced useful tools from an engineering point of view, such as the Moody chart, a plot that can be used to predict pressure drop or flow rate down a pipe. It shows that fluid flow in rough pipes could be described by four dimensionless quantities that collapse onto a series of lines: Reynolds number, pressure loss coefficient, diameter ratio of the pipe and the relative roughness of the pipe. Supersonic and hypersonic flows have a more complex flow physics compared with their incompressible counterpart because of the strong coupling between the velocity and thermal fields. The effect of distributed surface roughness in high-speed flows is much less known and only few studies are available, but thanks to the advancement of technology DNSs are becoming more and more possible; one example is the work of Modesti et al. [10] (Figure 3, that performed DNSs at different Mach and Reynolds numbers, covering both the transitionally and fully rough regime, of a supersonic turbulent channel flow over cubical roughness elements.

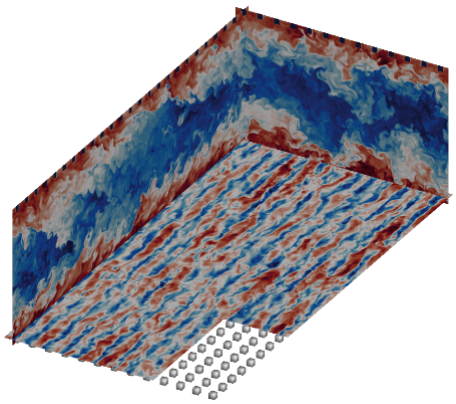

Figure 3: Image of the turbulent channel flow over cubical roughness elements taken from [10]

Supersonic flows over rough walls have so far been mainly studied experimentally, and even the

experimental studies are very limited in number.
Latin and Bowersox [8] conducted some experimental studies on a series of rough geometries, three sand grain roughened and two uniformly distributed rough surfaces with comparisons to a smooth surface. The distributed two-dimensional (2D) roughness elements were in the form of square shaped transverse bars and three-dimensional (3D) roughness elements in the form of cubes.
Williams et al. [19] performed a series of experiments of a hypersonic flow (the freestream Mach number was kept in the range 7.2 to 7.5) on a flat plate, with air as the working fluid. The experiment was carried out for two types of roughness geometry, one was a three dimensional diamond mesh type geometry, the other a two dimensional square bar geometry.
The latter is the work this thesis is based on, as it recreates the conditions of the flow, with some differences that will be explained later. Only the case with square bars was simulated, because the work is only at its preliminary stage, but the aim will be to extend the study to different types of roughness geometries.
Three Direct Numerical Simulations (DNS) of an hypersonic flow over a flat plate were performed. In the first case the surface of the plate is smooth, in the other two cases roughness is simulated with a series of square bars elements, whose characteristic dimensions are one the half of the other. The results of the two roughness cases will be compared with the smooth one in order to appreciate the effect of roughness on a series of variables such as velocity, density, temperature and boundary layer thickness.

The outline of the thesis is as follows: the first chapter is an overview of the basic theory of turbulent boundary layers, that shows the Navier-Stokes equation formulation, the governing equations of compressible boundary layers and of roughness in turbulent boundary layers and a synthesis of the main numerical method; the second chapter is dedicated to the computational setup and methodology, describing the solver STREAmS and the Immersed Boundary Method used in the simulations and the setup of the simulation itself; the last chapter shows the results of the simulations (instantaneous and mean fields and averaged and root mean square statistics).

4 Turbulent boundary layer - Mathematical approach

In this chapter an overview of the theory of the governing equations of boundary layers will be exposed, followed by a brief explanation of the numerical approach and the fluid-structure interface modeling used in the simulations.

4.1 Compressible Navier-Stokes equations

The flow is here idealized as a compressible ideal gas, and it is described using the Navier-Stokes equations. It is a system of three equations, which respectively describe the mass, momentum and energy conservation.

4.1.1 Conservation of mass

The conservation of mass states that the rate of change with time of mass in a certain control volume is zero. This concept can be written as:

$$\frac{d}{dt}m_s = 0 \quad \text{where} \quad m_s = \int_V \rho dV \tag{4.1}$$

Using the Reynolds transport theorem for the function $\rho(\vec{x}, t)$ we obtain:

$$\frac{d}{dt}\int_V \rho dV = \int_V \frac{\partial \rho}{\partial t} dV + \int_{\delta V} \rho \vec{u} \cdot \vec{n} dS = 0 \tag{4.2}$$

Using the divergence theorem on the second term

$$\int_V \frac{\partial \rho}{\partial t} dV + \int_V \vec{\bigtriangledown} \cdot (\rho \vec{u}) dV = \int_V \left[\frac{\partial \rho}{\partial t} + \vec{\bigtriangledown} \cdot (\rho \vec{u}) \right] dV = 0 \tag{4.3}$$

Which leads to the law of conservation of mass in the conservative form:

$$\frac{\partial \rho}{\partial t} + \vec{\bigtriangledown} \cdot (\rho \vec{u}) = 0 \tag{4.4}$$

or, using the index notation,

$$\frac{\partial \rho}{\partial t} + \frac{\partial \rho u_j}{\partial x_j} = 0 \tag{4.5}$$

4.1.2 Conservation of momentum

the rate of chance of the momentum $\vec{Q}$ is given by the sum of the external forces, which can be divided in volume forces and surface forces.

$$\frac{d\vec{Q}}{dt} = \sum \vec{F_e} \quad \text{with} \quad \vec{Q} = m\vec{u} = \int_V \rho \vec{u} dV \tag{4.6}$$

Applying first the Reynolds transport theorem and then the divergence theorem the equation becomes:

$$\frac{d}{dt}\int_V \rho \vec{u} dV + \int_A \rho \vec{u}\vec{u} \cdot \hat{n} = \int_V \frac{\partial \rho \vec{u}}{\partial t} dV = \sum \vec{F_e} \tag{4.7}$$

$$\int_V \left[\frac{\partial \rho \vec{u}}{\partial t} \vec{\bigtriangledown} \cdot (\rho \vec{u}\vec{u}) \right] dV = \sum \vec{F_e} \tag{4.8}$$

The external forces can be divided in mass or volume forces and surface forces

$$\sum \vec{F_e} = \begin{cases} dF_{e,V} = \rho \vec{f} dV \\ dF_{e,A} = \vec{t_n} dA = \vec{\vec{T}} \cdot \hat{n} dA \end{cases} \tag{4.9}$$

The tensor $\vec{\vec{T}}$ has the following expression (for newtonian fuids):

$$\vec{\vec{T}} = -p\vec{\vec{I}} + 2\mu\vec{\vec{E}} + \lambda(\vec{\bigtriangledown} \cdot \vec{u})\vec{\vec{I}} \tag{4.10}$$

Putting together these expression and observing that the volume V is arbitrary, the equation becomes:

$$\frac{\partial \rho \vec{u}}{\partial t} + \vec{\bigtriangledown} \cdot (\rho \vec{u}\vec{u}) = \rho \vec{f} + \vec{\bigtriangledown} \cdot \vec{\vec{T}} \tag{4.11}$$

which represents the second of the Navier-Stokes equations.

$$\frac{\partial \rho \vec{u}}{\partial t} + \vec{\bigtriangledown} \cdot (\rho \vec{u}\vec{u}) = \rho \vec{f} - \vec{\bigtriangledown} p + \vec{\bigtriangledown} \cdot \vec{\Sigma} \tag{4.12}$$

In index notation:

$$\frac{\partial \rho u_i}{\partial t} + \frac{\partial \rho u_i u_j}{\partial x_j} = p f_i + \frac{\partial}{\partial x_j}\left(-p\delta_{ij} + \Sigma_{ij}\right) \tag{4.13}$$

4.1.3 Conservation of energy

The first principle of thermodynamics is the law of conservation of mass, that states that the time variation of the total energy of the system E_T is equal to the sum of the amount of heat transmitted to the system Q and the total work done to the system L.

$$\frac{d}{dt} E_T = \dot{Q} + \dot{L} \tag{4.14}$$

The total energy of the system is defined as the sum of internal and kinetic energy

$$E_T = \int_V \rho e_T = \int_V \rho \left(c_v T + \frac{1}{2} v^2 \right) dV \tag{4.15}$$

Using the Reynolds transport theorem the law becomes

$$\frac{d}{dt} \int_V \rho e_T dV + \int_A \rho e_T \vec{u} \cdot \hat{n} dA = \int_Q d\dot{Q} + \int_L d\dot{L} \tag{4.16}$$

Where $d\dot{Q}$ and $d\dot{L}$ can both be divided in volume and surface parts

$$d\dot{Q} = \begin{cases} d\dot{Q}_v = \rho \dot{Q}_v dV \\ d\dot{Q}_s = \dot{Q}_s dA = -(\vec{q} \cdot \hat{n}) dA \end{cases} \tag{4.17}$$

$$d\dot{L} = \begin{cases} d\dot{L}_v = \vec{u} \cdot d\vec{F}_v = \vec{u} \cdot (\rho \vec{f}) dv \\ d\dot{L}_s = \vec{u} \cdot \vec{t}_{(\hat{n})} dA = \vec{u} \cdot \vec{\vec{T}} \cdot \hat{n} dA \end{cases} - \tag{4.18}$$

Substituting these two definitions in 4.16 and differentiating we obtain:

$$\frac{\partial \rho e_T}{\partial t} + \vec{\bigtriangledown} \cdot (\rho e_t \vec{u}) = \rho \dot{Q} - \vec{\bigtriangledown} \cdot \vec{q} + \rho \vec{u} \cdot \vec{f} + \vec{\bigtriangledown} \cdot \left(\vec{u} \cdot \vec{\vec{T}} \right) \tag{4.19}$$

Other relations:

$$e_T = c_v T + \frac{u^2}{2}$$

$$\vec{q} = -k\vec{\bigtriangledown}T$$

$$\vec{\vec{E}} = \frac{\vec{\bigtriangledown}\vec{u} + \vec{\bigtriangledown}\vec{v}^T}{2}$$

In index notations:

$$\rho\left(\frac{\partial e_T}{\partial t} + v_j\frac{\partial e_T}{\partial x_j}\right) = \rho\dot{Q} - \frac{\partial q_i}{\partial x_i} + \rho u_i f_i - \frac{\partial p u_i}{\partial x_i} + \frac{\partial}{\partial x_j}\left(u_i\Sigma_{ij}\right) \tag{4.20}$$

Navier-Stokes in index notation:

$$\begin{cases} \frac{\partial\rho}{\partial t} + \frac{\partial\rho u_j}{\partial x_j} = 0 \\ \\ \frac{\partial\rho u_i}{\partial t} + \frac{\partial\rho u_i u_j}{\partial x_j} = p f_i + \frac{\partial}{\partial x_j}\left(-p\delta_{ij} + \Sigma_{ij}\right) \\ \\ \rho\left(\frac{\partial e_T}{\partial t} + v_j\frac{\partial e_T}{\partial x_j}\right) = \rho\dot{Q} - \frac{\partial q_i}{\partial x_i} + \rho u_i f_i - \frac{\partial p u_i}{\partial x_i} + \frac{\partial}{\partial x_j}\left(u_i\Sigma_{ij}\right) \end{cases} \tag{4.21}$$

4.2 Compressible boundary layer

4.2.1 Equations

The resolution of the Navier-Stokes equations can have some difficulties and that is why they are usually simplified with the use of some assumption. For example Euler assumes that for high Reynolds numbers the viscous terms can be neglected, and he obtains a system of two equations that describes the flow. There are some problems to this solution that can be solved whit the introduction of the concept of *boundary layer*. It consists in a small region adjacent to the wall, where viscous effects and high flux gradients can not be neglected.
Inside this region the velocity has high gradients, as it goes from zero at the wall to the value imposed by the external solution at the edge of the boundary layer.
An important aspect to be considered is the fact that the boundary layer thickness grows along the streamwise direction, x. At first the velocity profile depends on the initial condition, but after a certain point the profile is independent from the initial solution and it just grows in the normal direction with respect to the wall without changing shape (Blasius).
There are several formal definitions of the boundary layer thickness in literature. The first is $\delta_9 9$, that considers the boundary layer thickness as the normal distance from the wall to which the streamwise velocity is equal to 99% of the undisturbed one. Another important definition is the displacement thickness δ^*, that considers an equivalent system in the external solution that has the same mass flux as the internal one. It represents the distance to which the external solution should be moved to get the same mass flux of the real solution through the boundary layer, and its mathematical definition is

$$\delta^+ = \int_0^h 1 - \frac{u}{u_{e,0}} dy \tag{4.22}$$

where h is the distance from the wall of a point outside the boundary layer and $u_{e,0}$ is the velocity of the external solution.

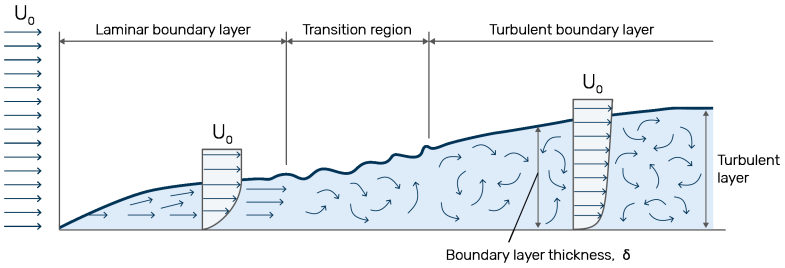

Figure 4: Development of the kinematic boundary layer on a flat plate

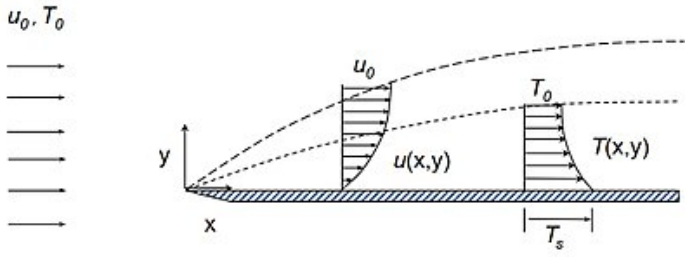

Figure 5: Kinetic and thermal boundary layer thickness over a flat plate

In a flat plate the boundary layer thickness $\delta(x)$ can be expressed as a function of the streamwise coordinate x, whose origin is on the leading edge of the plate, and its Reynolds number can defined as

$$Re_x = \frac{u_{e,0}}{\nu} x \tag{4.23}$$

where ν is the kinematic viscosity. It is directly proportional to x, which means that it increases along the x direction. So, the domain can be divided into several different regions along the x direction (Figure 4), according to the Reynolds number:

- $Re_x < 10$: the viscous effects are comparable to the inertial ones, which means that the boundary layer is not formed yet and there is no difference between the external and the internal solution.
- $10 < Re < 10^3$: the boundary layer has formed and it has a laminar nature. The velocity profile depends on the initial condition $u_{x_o}(y)$.
- $10^3 < Re < 10^6$: it's called the *similarity region* and the velocity profile is independent from the initial condition.
- $Re > 10^6$: the flow becomes turbulent, three-dimensional and non stationary, creating vortexes

There exists another kind of boundary layer, called *thermal boundary layer* (Figure 5). It is that region in which the diffusive terms are comparable to the convective terms and it is as thinner as the velocity is higher. When a body is immersed in a fluid in motion that has a lower temperature than the body itself, the temperature field is not uniform because the portion of fluid influenced by the difference of temperature between fluid and body is flattened in the streamwise direction and is reduced to a thin layer near the wall and in the wake of the body.

Let's consider the Navier-Stokes equation of a bi-dimensional stationary and incompressible flow. The system becomes:

$$\begin{cases} \frac{\partial u}{\partial x} + \frac{\partial v}{\partial y} = 0 \\ u\frac{\partial u}{\partial x} + v\frac{\partial u}{\partial y} = -\frac{1}{\rho}\frac{\partial P}{\partial x} + \nu\left(\frac{\partial^2 u}{\partial x^2} + \frac{\partial^2 u}{\partial y^2}\right) \\ u\frac{\partial v}{\partial x} + v\frac{\partial v}{\partial y} = -\frac{1}{\rho}\frac{\partial P}{\partial x} + \nu\left(\frac{\partial^2 v}{\partial x^2} + \frac{\partial^2 v}{\partial y^2}\right) \\ \rho u\frac{\partial h}{\partial x} + \rho v\frac{\partial h}{\partial y} = u\frac{\partial p}{\partial x} + v\frac{\partial p}{\partial y} + \frac{\mu}{Pr}\left(\frac{\partial^2 h}{\partial x^2} + \frac{\partial^2 h}{\partial y^2}\right) + 2\mu\left[\left(\frac{\partial u}{\partial x}\right)^2 + \left(\frac{\partial v}{\partial y}\right)^2 + \left(\frac{\partial u}{\partial y}\frac{\partial v}{\partial x}\right)^2\right] \end{cases} \tag{4.24}$$

The aim is to find the dimension of the boundary layer thickness δ as a function of the Reynolds number compared to the reference length L. The diffusive term must balance the convective one. The convective and diffusive terms of the second equation can be written in adimensional form respectively as:

$$u\frac{\partial u}{\partial x} \sim U_\infty \frac{U_\infty}{L} \tag{4.25}$$

$$\nu\frac{\partial^2 u}{\partial x^2} \sim \nu\frac{U_\infty}{L^2} \tag{4.26}$$

$$\nu\frac{\partial^2 u}{\partial y^2} \sim \nu\frac{U_\infty}{\delta^2} \tag{4.27}$$

Comparing the order of magnitude of these terms:

$$\nu\frac{\partial^2 u}{\partial x^2} / u\frac{\partial u}{\partial x} \sim \nu\frac{U_\infty L}{L^2 U^2{}_\infty} = \frac{\mu}{U_\infty L} = \frac{1}{Re} << 1 \tag{4.28}$$

For high Reynolds numbers the diffusive term is much smaller than the convective one, therefore its not the one that balances the equation.

$$\nu\frac{\partial^2 u}{\partial y^2} / u\frac{\partial u}{\partial x} \sim \frac{U_\infty L}{\delta^2 U^2{}_\infty} = \frac{L^2\mu}{\delta^2 U_\infty Re} = \frac{L^2}{\delta^2}\frac{1}{Re} \tag{4.29}$$

This value depends on the dimension of δ with respect to L, even for high Reynolds numbers. It is a finite value only if $\frac{\delta}{L}$ has the same order of magnitude as $Re^{\frac{1}{2}}$, so we can assume:

$$\frac{\delta}{L} = \frac{1}{\sqrt{Re}} \tag{4.30}$$

Let's consider the continuity equation terms:

$$\frac{\partial u}{\partial x} \sim \frac{U_\infty}{L}$$
$$\frac{\partial v}{\partial y} \sim \frac{V_\infty}{\delta}$$

They are comparable only if:

$$\frac{V_\infty}{\delta} / \frac{U_\infty}{L} \sim 1$$

which implies:

$$V_\infty = \frac{U_\infty}{\sqrt{Re}} \tag{4.31}$$

Applying this change in coordinates and using adimensional variables ($x^* = x/L, y^* = y/L, u^* = u/U_\infty . v^* = U_\infty, p^* = p/(\rho U_\infty)^2, h^* = h/U_\infty^2$) the incompressible 2D adimensional Navier-Stokes equations become

$$\begin{cases} \frac{\partial u^*}{\partial x^*} + \frac{\partial v^*}{\partial y^*} \\ u^* \frac{\partial u^*}{\partial x^*} + v^* \frac{\partial u^*}{\partial y^*} = -\frac{\partial p^*}{\partial x^*} + \frac{1}{Re}\left(\frac{\partial^2 u^*}{\partial x^{*2}} + \frac{\partial u^*}{\partial y^*}\right) \\ u^* \frac{\partial v^*}{\partial x^*} + v^* \frac{\partial v^*}{\partial y^*} = -\frac{\partial p^*}{\partial x^*} + \frac{1}{Re}\left(\frac{\partial^2 v^*}{\partial x^{*2}} + \frac{\partial v^*}{\partial y^*}\right) \\ u^* \frac{\partial h^*}{\partial x^*} + v^* \frac{\partial h^*}{\partial y^*} = u^* \frac{\partial p^*}{\partial x^*} + v^* \frac{\partial p^*}{\partial y^*} + \frac{1}{RePr}\left(\frac{\partial^2 h^*}{\partial x^{*2}} + \frac{\partial^2 h^*}{\partial y^{*2}}\right) + \frac{2}{Re}\left[\left(\frac{\partial u^*}{\partial x^*}\right)^2 + \left(\frac{\partial v^*}{\partial y^*}\right)^2 + \left(\frac{\partial u^*}{\partial y^*}\frac{\partial v^*}{\partial x^*}\right)^2\right] \end{cases} \tag{4.32}$$

In order to "zoom in" on what happens inside the boundary layer in the y direction it is useful to apply a change in coordinates with L and δ as reference length for the x and y direction respectively:

$$x' = \frac{x}{L} = x^*$$

$$y' = \frac{y}{\delta} = \frac{y}{L}\frac{L}{\delta} = y^* \sqrt{Re}$$

Consequently, non-dimensional equations of continuity and y-momentum become:

$$\begin{cases} \frac{\partial u'}{\partial x'} + \frac{\partial v'}{\partial y'} = 0 \\ \frac{1}{Re}\left(u' \frac{\partial v'}{\partial x'} + v' \frac{\partial v'}{\partial y'}\right) = -\frac{\partial p'}{\partial y'} + \frac{1}{Re^2}\frac{\partial^2 v'}{\partial x'^2} + \frac{1}{Re}\frac{\partial^2 v'}{\partial y'^2} \end{cases} \tag{4.33}$$

For high Reynolds numbers, $Re \to \infty$, the momentum equation is reduced to

$$\frac{\partial p'}{\partial x'} = 0$$

which means that p' is a constant of y, that implies $p' = p'(x)$. The fact that p' is constant along the y direction, together with the necessity of the pressure to recover the external solution, brings the junction condition for pressure:

$$\lim_{y' \to \infty} p'(x') = \lim_{y^* \to 0} p_e^*(x^*, y^*) = p_{e,0}^*(x^*) = p_{e,0}'(x') \tag{4.34}$$

Substituting this condition in the non-dimensional x-momentum equation, it becomes

$$u' \frac{\partial u'}{\partial x'} + v' \frac{\partial u'}{\partial y'} = -\frac{\partial p'}{\partial x'} + \frac{1}{Re}\frac{\partial^2 u'}{\partial x'^2} + \frac{\partial^2 u'}{\partial y'^2} \tag{4.35}$$

When $Re \to \infty$:

$$u' \frac{\partial u'}{\partial x'} + v' \frac{\partial u'}{\partial y'} = -\frac{\partial p_{e,0}'}{\partial x'} + \frac{\partial^2 u'}{\partial y'^2} \tag{4.36}$$

If we add the energy equation we obtain the final governing equations for an incompressible boundary layer:

$$\begin{cases} \frac{\partial u'}{\partial x'} + \frac{\partial v'}{\partial y'} = 0 \\ \frac{\partial p'}{\partial y'} = 0 \\ u' \frac{\partial u'}{\partial x'} + v' \frac{\partial u'}{\partial y'} = -\frac{\partial p_{e,0}'}{\partial x'} + \frac{\partial^2 u'}{\partial y'^2} \\ u' \frac{\partial h'}{\partial x'} + v' \frac{\partial h'}{\partial y'} = -u' \frac{\partial p_{e,0}'}{\partial x'} + \frac{1}{Pr}\frac{\partial^2 h'}{\partial y'^2} + \left(\frac{\partial u'}{\partial y'}\right)^2 \end{cases} \tag{4.37}$$

These equations lend two boundary conditions for the u' component of the flow:

$$u'(x', y' = 0) = 0 \qquad \text{adherence condition} \tag{4.38}$$

$$\lim_{y' \to \infty} u' = U^*_{e,0}(x) \qquad \text{junction condition} \tag{4.39}$$

and one boundary condition for the v' component:

$$v'(x', y' \to 0) = 0 \qquad \text{impermeability condition} \tag{4.40}$$

In compressible flows, the kinematic and temperature fields are not independent.

The Navier-Stokes equations ca be written as

$$\begin{cases} \frac{D\rho}{Dt} + \bigtriangledown \cdot \mathbf{v} = 0 \\ \rho \frac{D\mathbf{v}}{Dt} + \bigtriangledown p' = \mu \bigtriangledown^2 \mathbf{v} + (\Lambda + \mu) \bigtriangledown (\bigtriangledown \cdot \mathbf{v}) + (\rho - \rho_\infty) g \\ \rho c_p \frac{DT}{Dt} = \bigtriangledown \cdot (\lambda \bigtriangledown T) + \frac{Dp}{Dt} + \mu \phi_v \end{cases} \tag{4.41}$$

where p' is the difference between the static and hydrostatic pressure, ϕ_v is the *viscous dissipation function*, the molecular viscosity μ, the thermal conductivity λ and the viscous coefficient Λ are constant.
This system can be rendered non-dimensional by introducing the non-dimensional variables:

$$x^* = \frac{x}{L_0}, \quad t^* = \frac{U_\infty}{L_0} t, \quad \mathbf{v}^* = \frac{\mathbf{v}}{U_\infty}, \quad \rho^* = \frac{\rho}{\rho_\infty}, \quad p^* = \frac{p'}{\rho_\infty U_\infty^2}, \quad T^* = \frac{T}{\Delta T_0} \tag{4.42}$$

where L_0 is the characteristic dimension of the body and $\Delta T = T_w - T_\infty$ (T_w is the temperature of the body. Being Re the Reynolds number (ratio between inertial and viscous forces), Fr the Froude number(square root of the ratio between inertial and gravitational forces) , Pr the Prandtl number (relation between kinematic and thermal boundary layer) and E the Eckert number (relation between kinetic energy and enthalpy), defined as:

$$Re = \frac{U_\infty L_0}{\nu}, \quad Fr = \frac{U_\infty}{\sqrt{g L_0}}, \quad Pr = \frac{\mu c_p}{\lambda}, \quad E = \frac{U_\infty}{c_p \Delta T_0} \tag{4.43}$$

the non-dimensional Navier-Stokes equations can be written as

$$\begin{cases} \frac{D\rho^*}{D^*t} + \rho^* \bigtriangledown \cdot \mathbf{v}^* = 0 \\ \rho \frac{D\mathbf{v}^*}{Dt^*} + \bigtriangledown p^* = \frac{1}{Re} \left[\bigtriangledown^2 \mathbf{v}^* + (1 + \frac{\Lambda}{\mu}) \bigtriangledown (\bigtriangledown \cdot \mathbf{v}^*) \right] + \frac{1}{Fr^2} (\rho^* - 1) \mathbf{j} \\ \rho \frac{DT^*}{Dt^*} = \frac{1}{PrRe} \bigtriangledown^2 T^* + E \frac{Dp^*}{Dt^*} + \frac{E}{Re} \phi_v \end{cases} \tag{4.44}$$

where $\mathbf{j}$ is the unit vector along the direction of the gravitational force.
For hypersonic flows, the Froude number high enough to neglect the gravitational terms. But at high M_∞ values the density variations caused by the temperature variations can no longer be neglected.

4.2.2 Viscous scales

In turbulent boundary layer flows the effect of viscosity enforces the no-slip boundary condition bringing the fluid velocity to zero at the wall. The role of kinematic viscosity μ and wall shear stress τ_w is more important close to the wall [14], and for this reason the *viscous scales* are defined, in order to scale parameters for velocity and wall-normal distance in this region.

The viscous-friction scaling will be denoted with the $^+$ superscript. The *friction velocity* and *viscous lengthscale* are defined as:

- Friction velocity: $u_\tau = \sqrt{\frac{\tau_w}{\rho}}$
- Viscous lengthscale: $\delta_v = \nu\sqrt{\frac{\rho}{\tau_w}} = \frac{\mu}{u_\tau}$

As a consequence a new type of Reynolds number can be defined, specific for the turbulent boundary layer, called the *friction Reynolds number*:

$$Re_\tau = \frac{u_\tau \delta}{\mu} = \frac{\delta}{\delta_v}$$

The wall-normal distance scaled by friction length scale is given in *wall units*, defined as

$$y^+ = \frac{y}{\delta_v} = \frac{u_\tau y}{\mu}. \tag{4.45}$$

Its magnitude can be expected to determine the relative importance of viscous and turbulent processes.
Different layers are defined based on y^+. This division is called the *Law of the wall*. Prandtl hypothesis for the law of the wall states that u^+ only depends on y^+

$$u^+ = f_w(y^+) \quad \text{with} \quad f_v(y^+) = \int_0^{y^+} \frac{1}{y'}\Phi_I(y')dy' \tag{4.46}$$

where Φ is a universal non-dimensional function.

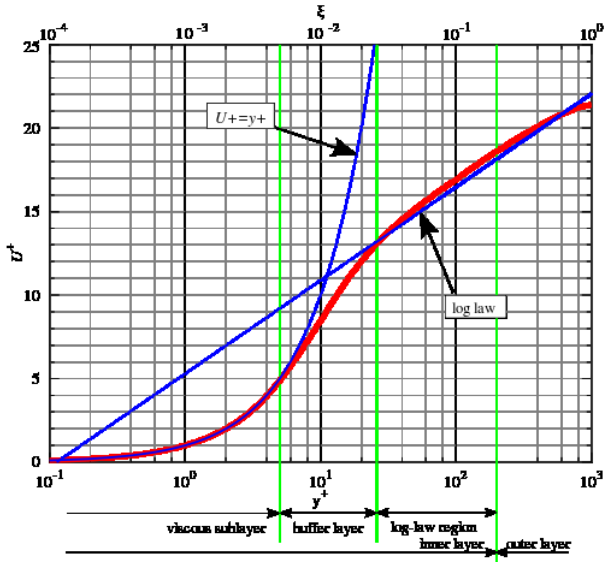

Figure 6: Law of the wall

The division, shown in Figure 6, is the following:

- *Viscous sublayer* $(0 < y^+ < 5)$
- *Log-law region* $(y^+ > 30)$
- *Buffer region* $(5 < y^+ < 30)$

As the Reynolds number increases, the dimensions of the viscous wall region decreases, since $\frac{\delta_v}{\delta}$ varies as ${Re_\tau}^{-1}$.
This regions will now be analyzed individually.

Viscous sublayer

It is the closest region to the wall. Here the Reynolds shear stress is negligible compared with the viscous stress.

In this layer the viscous forces are dominating and they produce the no-slip condition. Assuming that the shear stress is approximately constant and equivalent to the wall shear stress τ_w, we can obtain a linear relationship between the time-averaged velocity and the distance from the wall:

$$U^+ = y^+ \tag{4.47}$$

Logarithmic law

For large y^+ (higher than ~ 30), if the outer Reynolds number is sufficiently large, it can be supposed that the viscosity has little to no effects, so the dependence of Φ on the viscosity ν vanishes, and Φ adopts a constant value k^{-1}:

$$\Phi(y^+) = \frac{1}{k} \quad \text{for} \quad \frac{y}{\delta} << 1 \quad \text{and} \quad y^+ >> 1 \tag{4.48}$$

where $k(\approx 0.4)$ is the von Kármán constant.

The mean velocity gradient is

$$\frac{du^+}{dy^+} = \frac{1}{ky^+} \tag{4.49}$$

Integration of this equation leads to the formulation of the log law

$$u^+ = \frac{1}{k} \ln y^+ + B \tag{4.50}$$

where the log-law intercept B is universal for smooth walls ($k << 1$).

Buffer layer

It's the transition area between *Viscous sublayer* and *Log-law region*, where neither of the two laws apply
In the buffer layer the velocity profile doesn't follow neither the linear law nor the log-law, and there is no analytical description.
An empirical one is given by Van Driest: for a boundary layer with $\frac{\partial u}{\partial y} > 0$, according to the mixing length hypothesis, the total shear stress is

$$\begin{aligned}\frac{(y)}{\rho} &= \nu\frac{\partial u}{\partial y}\mu_t\frac{\partial u}{\partial y} \\ &= \nu\frac{\partial u}{\partial y} + {l_m}^2\left(\frac{\partial u}{\partial y}\right)^2 \quad \text{with} \quad {l_m}^+ = \frac{l_m}{\delta_\mu}\end{aligned} \tag{4.51}$$

Normalising this equation by viscous scales it becomes:

$$\frac{\tau}{\tau_w} = \frac{\partial u^+}{\partial y^+} + \left(l_m^+\frac{\partial u^+}{\partial y^+}\right)^2 \tag{4.52}$$

This is a quadratic equation for $\frac{\partial u^+}{\partial y^+}$ that has the following solution:

$$\frac{\partial u^+}{\partial y^+} = \frac{\frac{2\tau}{\tau_w}}{1+\sqrt{1+\frac{4\tau}{\tau_w}(l_m^+)^2}} \tag{4.53}$$

In the inner layer $\frac{\tau}{\tau_w} \simeq 1$, and this allow us to find the law of the wall:

$$u^+ = f_w(y^+) = \int_0^{y^+}\frac{2dy'}{1+\sqrt{1+4l_m^+(y')^2}} \tag{4.54}$$

The specification for the mixing length in the logarithmic region is $l_m = ky$ ($l_m^+ = ky^+$). Using the same specification in the viscous sublayer, the implied turbulent stress $\nu_t\frac{\partial\langle U\rangle}{\partial y}$ would increase as y^2, whereas $-\langle\rho uv\rangle$ would increase more slowly, as y^3. This implies that the specification $l_m = ky$ has to be damped near the wall:

$$l_m^+ = ky^+\left[1-e^{\frac{-y^+}{A^+}}\right] \quad \text{with} \quad A^+ = 26 \tag{4.55}$$

The term inside the square brackets is the *Van Driest damping function*, which tends to unity for high values of y^+, allowing the log-law to be recovered.

For $\frac{y}{\delta} > 0.2$ the mean velocity deviates from the log-law. To describe this phenomenon it is necessary to use another function that will be summed to the law of the wall:

$$\frac{\langle U\rangle}{u_\tau} = f_w\left(\frac{y}{\delta_v}\right) + \frac{\Pi}{k}w\left(\frac{y}{\delta}\right) \tag{4.56}$$

The function $w\left(\frac{y}{\delta}\right)$ is called the *wake function* and is defined to satisfy the normalization conditions $w(0) = 0$ and $w(1) = 2$. An approximation of the wake function could be:

$$w\left(\frac{y}{\delta}\right) = 2sin^2\left(\frac{\pi}{2}\frac{y}{\delta}\right) \tag{4.57}$$

Π is a non-dimensional quantity called *wake strength parameter*, whose value is flow dependent. The shape of the function $w\left(\frac{y}{\delta}\right)$ is similar to the velocity profile in a plane wake, with a symmetry plane at y=0.

$$\frac{U_0-\langle U\rangle}{u_\tau} = \frac{1}{k}\left\{-\ln\frac{y}{\delta} + \Pi\left[2-w\left(\frac{y}{\delta}\right)\right]\right\} \tag{4.58}$$

4.3 Roughness

All predictive models rely on an important assumption, proposed by Townsend (1956, p. 89) and articulated by Raupach et al. (1991), that smooth- and rough-wall turbulence behave similarly away from the wall. Specifically, this similarity hypothesis states that friction-scaled turbulent relative motions in the outer layer, such as the mean velocity defect and covariances of velocity fluctuations, are independent of surface condition at sufficiently high Reynolds number and sufficiently large scale separation.

4.3.1 Incompressible

According to [12] who conducted experiments on the flow of water in pipes roughened by sand, we can identify three conditions in the flow where the resistance to the flow of water is dependent on the average roughness height k. For small values of k, compared with , the rough wall is inside the viscous sub-layer and the resistance to the flow given by the rough wall is similar to the smooth wall. This type of surface is called *hydraulically smooth*. When k is comparable to , the resistance to the water flow is bigger and the behaviour of the wall changes from smooth to rough, Which is why this behaviour is defined *transitionally rough*. As the Reynolds number increases, the resistance increases. When the value of k is bigger than , the wall becomes *fully rough* the Reynolds number doesn't influence the resistance to the flow of water.
One important concept to consider is the Townsend outer layer similarity hypothesis [15]. This similarity hypothesis states that friction-scaled turbulent relative motions in the outer layer, such as the mean velocity defect and covariances of velocity fluctuations are independent of surface condition at sufficiently high Reynolds number (i.e., when the outer-layer thickness is greater than the viscous wall unit) and sufficiently large scale separation ($\delta >> k$). The direct effect of roughness is confined to the roughness sublayer (y $<$ yr), where yr is the height of the roughness sub-layer, and roughness only sets the boundary condition, namely the friction velocity u for the outer flow of thickness .

The smooth wall and rough wall are similar away from the wall. The effect of roughness is confined to a region very close to the wall, for values of y smaller than the height of the roughness sub-layer.
In order to assure the separation of scales it is necessary that $\frac{k}{\delta} < \frac{1}{40}$ ([6]), which derives from the assumption that roughness directly influences up to $y_r = 3k$ of the flow, so this region will be below half of the thickness of the log layer. Roughness causes a downward shift in the logarithmic layer of the viscous scaled mean velocity profile, known as the Hama roughness function $\Delta U^+ = \Delta U/u_\tau$. In the hydraulically smooth regime, the logarithmic law of the wall relation holds

$$\langle u_s \rangle^+ = \frac{1}{k} \log\left(y^+\right) + B \tag{4.59}$$

where the subscript "s" indicates smooth-wall conditions, so $\langle u_s \rangle^+$ and y^+ respectively are the smooth wall mean-velocity and wall normal coordinate. Increasing the value of k^+, known as the roughness Reynolds number, that is calculated based on the height k of the roughness element ($k^+ = ku_\tau/\nu$), the logarithmic law becomes

$$\langle u_r \rangle^+ = \frac{1}{k} \log\left(\frac{y}{k}\right) + B_R(k^+) \tag{4.60}$$

where $\langle u_r \rangle^+$ is the mean velocity of the rough wall. The difference is in the term $B_R(k^+)$ which is no longer a constant, but depends on the roughness Reynolds number and the roughness

topography. For smooth walls we could neglect viscous effects in setting the intercept B, but for $k^+ >> 1$ the intercept B approaches a finite value B_R that is independent of roughness Reynolds number but depends only on the roughness topography.
The outer-layer similarity ($y >> \nu/u_\tau$,k) is one necessary condition to obtain the log laws of equations 4.59 and 4.60. For this reason, the appearance of a log law has often been taken as evidence of outer-layer similarity ([2]). However, an additional condition for logarithmic behavior is $y << \delta$, while Townsend's outer-layer similarity requires only $y < \delta$.
A convenient and intuitive way to describe the log-law intercept B(k^+) is through the roughness function $\Delta U^+(k^+)$, defined independently by Clauser (1954) and Hama (1954) and given by the shift at matched y^+ of the rough-wall log law (Equation 4.60) relative to that of the smooth wall (Equation 4.59):

$$\Delta U^+(k^+) = U_s^+ - U_R^+ = \frac{1}{k}\log(k^+) + B - B(k^+) \tag{4.61}$$

The downward shift in the mean velocity profile causes a momentum deficit that derives from the surface roughness. Thus the roughness function ΔU^+ can be interpreted as a measure of the drag penalty relative to a smooth wall, that corresponds to an increase in drag when $\Delta U^+ > 0$. $\Delta U^+(k^+)$ can be different for every rough surface, not only in the value of the fully rough intercept B_R but also in the behavior of the transitionally rough regime. For this reason the prediction of drag due to rough surfaces is difficult and more studies need to be done in order to comprehend the flow behaviour in roughness conditions.

4.3.2 Compressible - Aerodynamic heating

Aerodynamic heating is the heating of a surface as a result of the high speed flow of air that passes over that surface. This heating is caused by friction of the fluid on the surface that generates heat and by the conversion of kinetic energy of motion into heat inside a thin layer of fluid [16]. Because of this, it appears that a "thermal barrier" exists over the surface , which can be overcome by proper engineering designs. The thermal barrier is similar to the sonic (drag) barrier, with the difference that the sonic barrier appears over a certain value of the Mach number, whereas the thermal barrier simply increases in intensity as the Mach number increases.
One of the important aspects when studying hypersonic flows is to characterize the heat transfer at the surface due to viscous heating. A non-dimensional parameter known as the Stanton number is used to characterize the rate of heat transfer at the wall. The Stanton number is the ratio of the heat transfer coefficient to the thermal capacity of the fluid. It is given by

$$S_t = \frac{q_w}{\rho u C_p (T_w - T_r)} \tag{4.62}$$

where q_w is the T_r is the recovery temperature given by

$$T_r = T\left[1 + \frac{\gamma - 1}{2} r M^2\right] \tag{4.63}$$

where T and M respectively are the temperature and Mach number of the external flow, r is the *recovery factor*, a constant that characterizes the amount of kinetic energy recovered from the flow, and $\gamma = c_p/c_v$ is the ratio of the specific heat at constant pressure (c_p) to the specific heat at constant volume (c_v). The stagnation temperature T_0 of a fluid is the temperature that that the fluid would reach if it was isentropically brought to rest on the wall from the outer flow. But since the process is not isentropic, the recovery temperature is defined as the temperature the

fluid attains when it is brought to rest on a wall from the viscous region. These two temperatures are different because not all of the kinetic energy is dissipated. The recovery factor is given as

$$r = \frac{T_r - T}{T_0 - T} \tag{4.64}$$

This is the reason why it is called *cold wall*, because the temperature that the fluid reaches at the wall is minor than the temperature it could reach if the process was isentropic.

4.4 Numerical methodology

Numerical simulations are required to study the behaviour of systems whose mathematical models are too complex to provide analytical solutions, as in most nonlinear systems.

- Direct Numerical Simulations (DNS): Direct numerical simulation (DNS) is used to solve instantaneous Navier–Stokes equations, resolving all scales, down to Kolmogorov dissipation scales, without using any models. It can give the most accurate results, with high spatial and temporal resolution, which cannot even be given by measurements. However, its computer requirements are extremely high, and increase rapidly with Reynolds number. Therefore, its application is limited to low-Reynolds number flows and small-size computation domains. The result of a DNS con be compared with a physical experiment with the same conditions.

- Large Eddy Simulations (LES): The statistics of the largest scales are dependent on the geometry of the fluid system while the statistics of the small scales are universal. For this reason in LES the large scale motions (large eddies) of turbulent flow are computed directly and only small scale (sub-grid scale (SGS)) motions are modelled, resulting in a significant reduction in computational cost compared to DNS

- Reynolds-Avareged Navier-Stokes (RANS) : It is a numerical method to model a turbulent flow wherein the flow quantities are decomposed into their time-averaged and fluctuating components (Reynolds decomposition). Therefor they only resolve the mean flow while all the turbulent scales are treated with an a priori model.

A complete description of a turbulent flow, where the flow variables are known as a function of time and space can be obtained by numerically solving the Navier-Stokes equations by using Direct Numerical Simulations (DNS in short). The instantaneous range of scales in turbulent flows increases rapidly with the Reynolds number. As a result, most engineering problems have too wide a range of scales to be directly computed using DNS [11].
The range of scales that need to be accurately represented in a computation is dictated by the physics. The grid determines the scales that are represented, while the accuracy with which these scales are represented is determined by the numerical method. The Kolmogorov length scale, $\eta = (\mu^3/\epsilon)^{\frac{1}{4}}$, is commonly quoted as the smallest scale that needs to be resolved. However, this requirement is probably too stringent. The smallest resolved lengthscale is required to be of $O(\eta)$, not equal to η. It appears that the relevant requirement to obtain reliable first and second order statistics is that the resolution be fine enough to accurately capture most of the dissipation. The smallest lengthscale that must be accurately resolved depends on the energy spectrum, and is typically greater than the Kolmogorov lengthscale

5 Computational setup and methodology

5.1 STREAmS

In this work, the solver used is STREAmS (Supersonic TuRbulent Accelerated navier-stokes Solver), developed by the research group at the Sapienza University of Rome. STREAmS has been tailored to canonical compressible turbulent wall-bounded flows, including channels, supersonic and hypersonic boundary layers, and shock wave/turbulent boundary layer interactions. This software presents significant advantage in terms of reduced computational effort, although limited to the simple geometrical configurations handled by STREAmS.[1]
Space discretization
The convective terms in the Navier–Stokes equations are discretized using a hybrid energy-preserving/shock-capturing scheme in locally conservative form. Being f_x the convective flux in the x direction, defined as

$$f_x = u\phi \tag{5.1}$$

where ϕ is the transported quantity ($\phi = 1$ for the mass equation, $\phi = u_j$ in the momentum equation and $\phi = H$, total enthalpy, for the energy equation), the numerical discretization of the streamwise derivative of the flux on a uniform mesh can be is

$$\left.\frac{\partial f_x}{\partial x}\right|_i = \frac{1}{\Delta x}\left(\hat{f}_{x,i+1/2} - \hat{f}_{x,i-1/2}\right) \tag{5.2}$$

where Δx is the spacing of the mesh. Let us define the three-point average operators as

$$\widetilde{(F,G,J)}_{i,l} = \frac{1}{8}(F_i + F_{i+l})(G_i + G_{i+l})(J_i + J_{i+l}) \tag{5.3}$$

The energy-preserving numeric flux at the interface $i + 1/2$ is obtained by rewriting in conservative form the split formulation of the Eulerian fluxes

$$\hat{f}_{x,i+1/2} = 2\sum_{l=1}^{L} a_l \sum_{m=0}^{l-1} \widetilde{(p,u,\phi)}_{i-ml} \tag{5.4}$$

where the a_l are the standard coefficients for central finite difference of the first derivative, with order of accuracy 2 L.
In smooth and shock-free regions of the flow an energy-consistent flux is applied, in order to guarantee that the total kinetic energy is discretely conserved in the limit case of inviscid incompressible flow. The order of accuracy of the discretization ranges from the second up to the eighth order and can be chosen by the user. The locally conservative formulation allows straightforward hybridization of the central flux with classical shock-capturing reconstructions. In this case, the Lax–Friedrichs flux vector splitting is used to ensure shock capturing capabilities, and the components of the positive and negative characteristic fluxes are reconstructed at the interfaces using a Weighted Essentially Non-Oscillatory (WENO) reconstruction. Similarly to the central flux, the order of accuracy of the shock capturing scheme can be changed from first to seventh order. The local smoothness of the numerical solution and switch between the energy preserving and the shock capturing discretization are judged by means of the use of a modified version of the Ducros shock sensor

$$\theta = max\left(\frac{-\bigtriangledown \cdot u}{\sqrt{\bigtriangledown \cdot u^2 + \bigtriangledown \times u^2 + u_0^2/L_0}}, 0\right) \in [0,1] \tag{5.5}$$

where u_0 and L_0 are velocity and length scales, which remain fixed during the simulation; for boundary layer they are the free-stream velocity and the inflow boundary layer thickness. The sensor is designed to be $\theta \approx 0$ in smooth flow regions and $\theta \approx 1$ in the presence of shock waves. The viscous terms are expanded to Laplacian form in order to avoid odd-even decoupling phenomena and approximated with a central finite-difference scheme. At the i-th node, the numerical discretization of the spatial derivative of the viscous fluxes in the x direction becomes

$$\begin{aligned} \frac{\partial}{\partial x}\left(\mu\frac{\partial u}{\partial x}\bigg|_i\right)\bigg|_i &= \frac{\partial \mu}{\partial x}\bigg|_i \frac{\partial u}{\partial x}\bigg|_i + \mu\frac{\partial^2 u}{\partial x^2}\bigg|_i \\ &= \frac{1}{\Delta x^2}\sum_{l=-L}^{L} a_l^2 \mu_{i+l} u_{i+l} + \frac{1}{\Delta x^2}\sum_{l=-L}^{L} b_l u_{i+l} \end{aligned} \tag{5.6}$$

where b_l are the the finite-difference coefficients for the second derivative of order 2L.

Time integration

The following semi-discrete system of ordinary differential equations is obtained from the discretization of the spatial derivatives:

$$\frac{\partial \mathbf{w}}{\partial t} = \mathbf{R}_{\mathbf{w}} \tag{5.7}$$

where $\mathbf{w} = [\rho.\rho u, \rho v, \rho w, \rho E]$ is the vector of the conservative variables and $\mathbf{R}$ the vector of the residuals.

The system is advanced in time using a three-stage, third-order Runge–Kutta scheme,

$$\mathbf{w}^{(s+1)} = \mathbf{w}^{(s)} + \alpha_s \Delta t \mathbf{R}^{(s-1)} + \beta_s \delta t \mathbf{R}^{(s)} \tag{5.8}$$

where s=0,1,2 is the sub-step, $w(0) = w(n)$ and $w(3) = w(n+1)$ are the solution respectively at the $n-th$ and $(n+1)-th$ steps, $\alpha_s = (0, 17/60, 5/12)$ and $\beta_s = (8/15, 5/12, 3/4)$ are the integration coefficients.

5.2 Immersed Boundary Method

The no-slip and no-penetration boundary conditions on the surface are imposed using the Immersed Boundary Method (IBM) [9]. which simulates the viscous flow with immersed boundaries, discretized with grids that do not conform to the shape of the object.The primary advantage of the IB method is associated with the fact that the task of grid generation is greatly simplified. Generating body-conformal structured or unstructured grid is usually very cumbersome. Even for simple geometries, generating a good-quality body-conformal grid can be an iterative process requiring significant input from the person generating the grid. Since the grid does not conform to the solid boundary, the boundary condition are introduced in the equation by a forcing function When working with compressible flows, the boundary conditions are defined as a gradient of some fluid variables. When employing a nonbody conformal Cartesian grid, the solid boundary would cuts through the volume grid, thus a Cartesian mesh can be employed independently of the geometry complexity or the motion of the boundary. Because the grid does not conform to the solid boundary, incorporating the boundary conditions would require modifying the equations in the vicinity of the boundary. Therefore, it is necessary to work with a method that can deal with both Dirichlet and Neumann boundary conditions. The

Ghost Point-Forcing Method (GPFM) [3] method is the one used by STREAmS and works with both boundary conditions.

The Ghost Point-Forcing Method imposes the boundary condition on the body interface using the ghost points: these are points in the solid that have at least one neighbour in the fluid region. For this reason the GPFM requires to discern if a computational node is a fluid, a ghost or a solid by using the *ray tracing algorithm*, an automatic solid-detection technique which is able to detect where a solid is located inside a grid of any type. The fundamental idea of Jordan's theorem [5] is to count the number of intersections between the solid bound and a semi-infinite ray in order to determine if a grid point is inside or outside a solid. Being $\sum$ a discrete representation of the three-dimensional solid surface, x_0 a grid point we want to discern if it is inside or outside $\sum$ and $\overline{x}$ a fixed point lying outside the computational domain. If $\overline{x}$ is sufficiently far from the domain, a semi-infinite ray starting from x0 can be approximated through the expression.

$$\mathbf{R}(t) = x_0 + (\overline{x} - x_0)t \qquad t \in [0:1] \tag{5.9}$$

If the flow is bi-dimensional the intersections with all elements in $\sum$ are identified by use of this ray is inside a loop. If the problem is three-dimensional a loop on all the triangles is performed and here a test is performed to check if the ray $\mathbf{R}(t)$ has an intersection with it. The problem can be faced employing a standard line-triangle intersections algorithm. Based on Jordan's theorem, if the total number of intersections is even, the grid point x_0 is outside the surface is identified as a fluid point; if the number of crossings is odd it is inside the surface and it's considered a solid point.
Once the distinction is made, to determine which are the ghost nodes the fluid points in the neighbourhood of a solid point are analyzed: if at least one fluid point is detected, the selected solid point is labelled as ghost point.

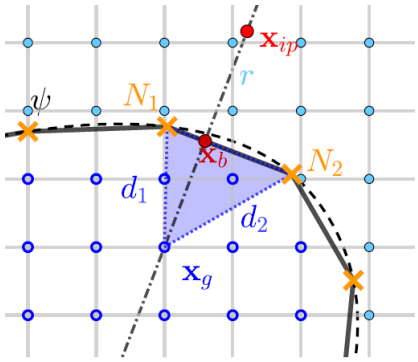

Figure 7: Sketch of the determination of the boundary point in respect of a ghost point. Here blue circle represent the ghost node, light blue points denotes the fluid region. Orange crosses represent the Lagrangian points

The next step is to impose the desired boundary condition at the fluid; in order to di so, the definition of the boundary and image points in the flow is necessary. Considering a ghost point x_g (Figure 7), first we identify the nearest Lagrangian points, then the line L passing through them and the relative orthogonal direction n are defined. The boundary point has to be on the orthogonal line to L, passing through the ghost point, which leads to the conclusion that this point corresponds to the intersection of the two lines. The location of the image point is determined using the expression

$$x_{in} = x_g + 2n_b\|x_b - x_g\| \tag{5.10}$$

where n_b is unit vector associated with the normal outer direction at the boundary location.

The last passage is the identification of the values of the flow field variables at each image point, which can be interpolated from the surrounding grid points. with this procedure we managed to impose the desired boundary conditions at the fluid-solid interface.

5.3 Setup

In this work three direct numerical simulations have been carried out on CINECA's Marconi100 cluster for three different roughness configurations. The simulations required the use of eight nodes, each one including 4 GPUs, which means that the parallel computing of the domain was executed on 32 GPUs. The in-house solver STREAmS is used, as mentioned above, to reproduces the flow behavior over the plate. The computational domain is configured as a square cuboid of size $100\delta_{in} \times 15\delta_{in} \times 9\delta_{in}$, discretized using a Cartesian non-body conformal, structured grid. The mesh features 5120 nodes in the x direction, 320 in the y direction and 512 in the z direction, for a total of 838.860.800 nodes. In order to better capture the behaviour of flow inside the boundary layer the grid is not uniform, but it's thicker near the wall. This is necessary when dealing with the strong gradients of the physical quantities that characterize the turbulent boundary layer, because a high number of nodes is required to resolve the boundary layer. The density of the nodes decreases moving away from the wall, and this non-uniform distribution of nodes permits to decrease the computational cost, but keeping a good resolution of the simulation.
Presently, x, y and z and u,v and w, respectively, correspond to the streamwise, wall-normal and spanwise directions and velocities.
The simulation are based on the experiment carried out by Williams et al. [19]. The experiments were conducted on a flat plate, with air as the working fluid. The maximum stagnation temperature is limited to about $800K$, so that the air always behaves as a perfect gas. The freestream Mach number was kept in the range 7.2 to 7.5 at the measurement location, depending on the configuration. To simulate the same conditions, the Mach number of the DNS is 7.25. The experiment was carried out for two roughness geometries, one was a three dimensional diamond mesh type geometry, the other a two dimensional square bar geometry. This work is limited to the analysis of the square bar roughness in two configurations. The values of the domain and of the bars are rendered adimensional dividing respectively for the boundary layer thickness at the inflow δ_{in} and for δ_ν.

The main problem encountered in this work was the difficulty in the computation of the wall shear stress τ_w in the two rough cases, because there isn't a method yet that permits to derive the value of τ_w on the roughness bar. If in future works such a method is computed, than the wall parameters such as Re_τ and u_τ could be known also for the rough cases.

Case	k^+	k/δ	λ/k
rough 1	15	0.06	5
rough 2	30	0.1	5

Table 1: Rough Simulations' parameters showing the topology of roughness elements

Case	k+	Mach	θ_{wall}	T_{inf}	$Re\tau_{in}$	domain
smooth	0	7.25	0.808	65.67 K	150	100x15x9 δ_{in}
rough 1	15	7.25	0.808	65.67 K	150	100x15x9 δ_{in}
rough 2	30	7.25	0.808	65.67 K	150	100x15x9 δ_{in}

Table 2: Simulations' parameters. $k^+ = k/\delta_\nu$, $\theta_w = (T_w - T_\infty)/(T_r - T_\infty)$, $Re_{\tau,in} = \delta_{in}/\delta\nu$, where δ_{in} if the inflow boundary layer thickness and the value of $\delta_\nu = 0.0077$ is taken for the smooth case.

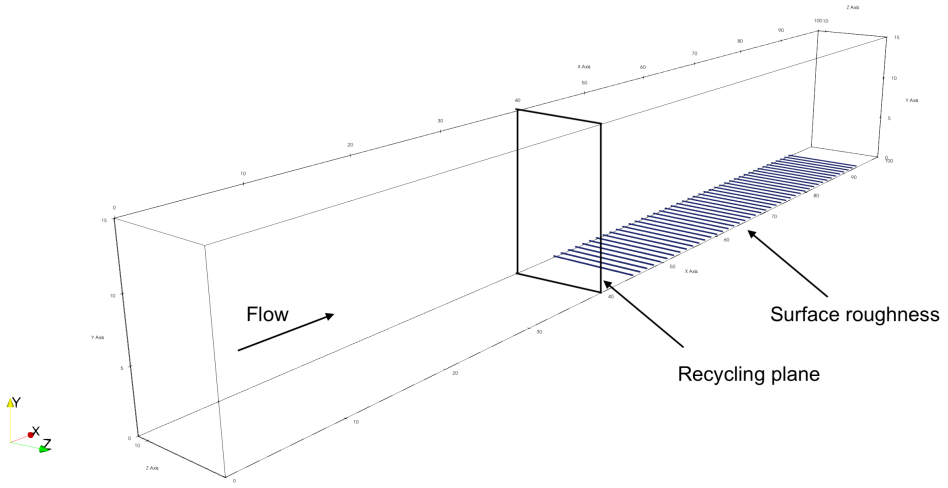

Figure 8: Sketch of the setup where you can see the flow direction, the initial smooth part followed by the recycling plane and the roughness elements on the flat plate where statistics are collected

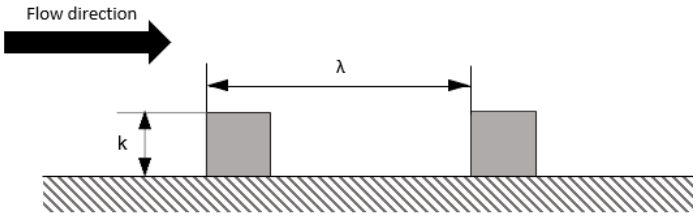

Figure 9: Topology of 3D roughness element depicted in side view

6 Results

Roughness in a compressible flow is not a thoroughly studied subject, as opposed to roughness in the an incompressible flow, that has been examined and for which a lot of theories are formulated, and the reason for this is that supersonic or hypersonic flows are more difficult to deal with because of the high temperatures at stake and of the behaviour of the boundary layer.
Therefore, the aim of this work is to study how an hypersonic flow reacts when it encounters a rough wall, by means of Direct Numerical Simulations of a Mach 7.5 flow over three different wall types, as explained in the previous chapter.

In this chapter a comparison between the three simulation's results will be exposed, paying particular emphasis to the dependence of the flow from the microstructure of the roughness elements. We will see from the results of these simulation that we can assume that the type of roughness only influence a small portion of the boundary layer, after which the flow only feels the increase in the boundary layer thickness. This means that the flow over a certain value of y/δ_{99} can be characterized by a single variable, but under that value the flow needs two variables to model, which makes it more complex.
In the following pages are shown the instantaneous fields of velocity, temperature, mach number and density in the wall-normal and wall-parallel plane and the mean density field for each of the three roughness layouts.

6.1 Wall-normal plane

The flow will be analyzed in its wall-normal and wall-parallel planes in order to fully describe its behaviour in the spanwise and streamwise directions. Let's consider the wall-normal plane first.

6.1.1 Instantaneous velocity field

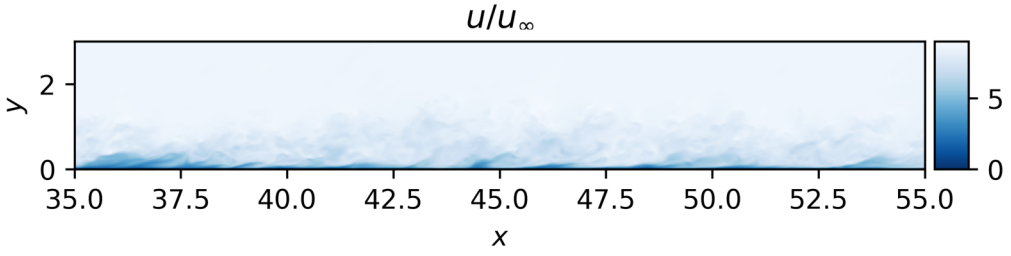

(a) $k^+ = 0$

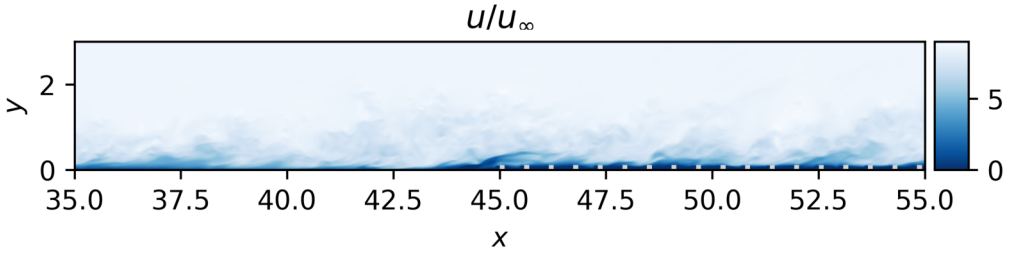

(b) $k^+ = 15$

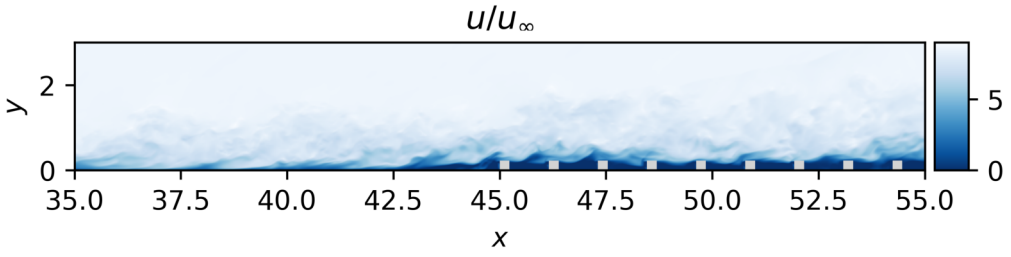

(c) $k^+ = 30$

Figure 10: Wall-normal slice of instantaneous field of velocity

Figure 10 shows the slice in the wall-normal plane of the instantaneous velocity field of the three flows in exam. It can be seen that the smooth case is mostly uniform, whereas in the two rough cases the flow significantly changes because of the presence of the roughness bars: the flow in the first half of the plate is almost identical to the smooth in each case; when it encounters the roughness bars it is characterized by a sudden decrease in velocity. From these images we can already assume the presence of a shock wave before the first roughness bar, that will be confirmed later by the analysis of the density field and the one dimensional profile of the boundary layer thickness in particular. The effect of the shock on the flow velocity appears evident in both the rough cases by noting that the velocity is very low right before the first roughness bar,

because the flow passes through the shock wave and its velocity decrease

The velocity of the flow in the region closest to the wall is almost zero. This area increases when roughness is present: the difference between the smooth case and the rough cases is evident in Figure 10. This phenomenon can be seen in both the rough cases in exam, but in the first case, where $k^+ = 15$, the effect of roughness is less evident than in the case with $k^+ = 30$. The latter has an extended region between the roughness bar in which the velocity is almost zero. The effect of the roughness elements on the velocity profile can also be seen in the one-dimensional graphics that will be shown later. The curves of the velocity profiles in the rough cases are shifted down and towards the right of the graphic, which means that the flow reaches lower velocities and at higher values of y/δ_{99}.
Another important aspect is the increase of the boundary layer height in both the rough cases: the slowed down flow takes longer to recover the velocity of the external solution, causing the boundary layer to increase in height.

6.1.2 Instantaneous temperature field

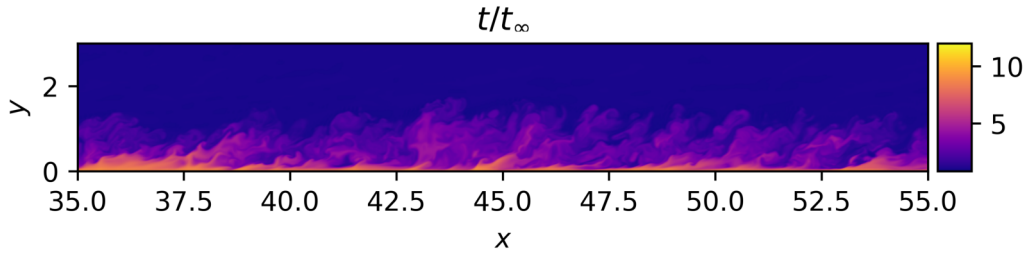

(a) $k^+ = 0$

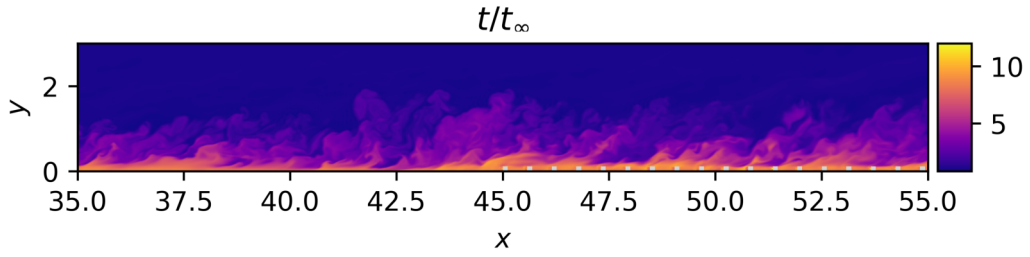

(b) $k^+ = 15$

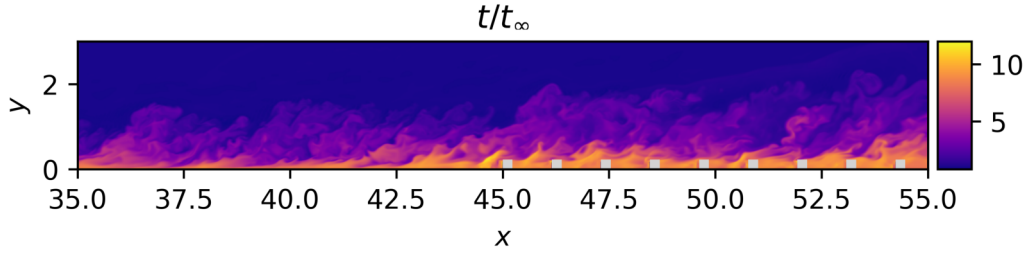

(c) $k^+ = 30$

Figure 11: Wall-normal slice of instantaneous field of temperature

In this paragraph the temperature of the flow is taken into account and examined by observing the wall-normal slices of its instantaneous fields.

The boundary layer in general is characterized by higher temperature than the outer flow, because inside the boundary layer the viscous stresses are relevant and they create heat, which causes the flow to reach high temperatures, particularly for hypersonic flows like the one in exam. Similarly to the velocity, the temperature at the wall gradually changes as one moves toward the free stream of the fluid, until it recovers the external temperature of the flow. The previously defined *thermal boundary layer* has some characteristics in common with the boundary layer, like the fact that the presence of the roughness elements causes the .
The temperature field of the smooth case, Figure 11 (a) is approximately uniform in the x direction, as one could have expected. The higher values of temperatures are reached at the wall, and some hot spots are visible. In the two rough cases the effects of the roughness elements are clearly visible, as the temperature reach even higher values than the smooth case. The areas between the roughness elements are the areas with higher temperatures. This can be observed in the first and in the second.
One other important aspect is the raising of the thermal boundary layer. From these images we can assume that, like in the case of the velocity field, the temperature takes more to recover the temperature of the external flow t_∞. This can be better observed in the one dimensional profiles, where the curves of the rough cases are shifted with respect to the curve of the smooth case.

6.1.3 Instantaneous Mach number field

In order to comprehend the behaviour of the flow it is useful to observe how the Mach number varies throughout the domain. In the following images, Figure 12, the white line corresponds to the unit value of Mach, so it is possible to learn in what areas the flow in subsonic.

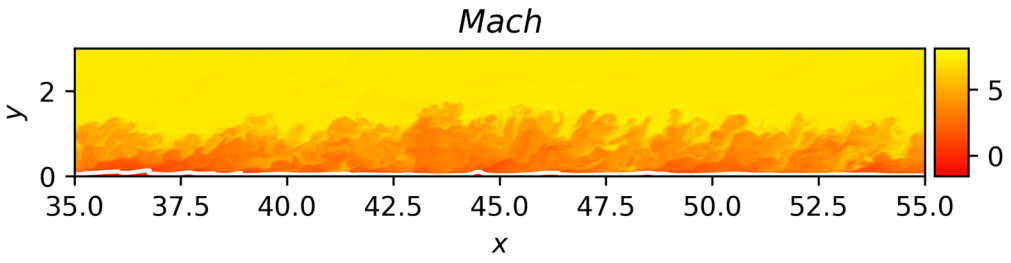

(a) $k^+ = 0$

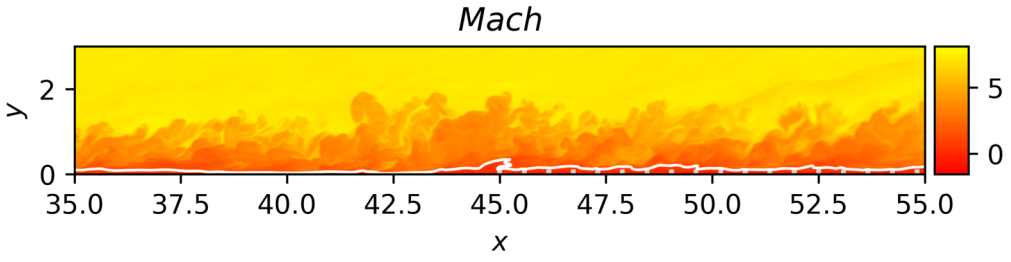

(b) $k^+ = 15$

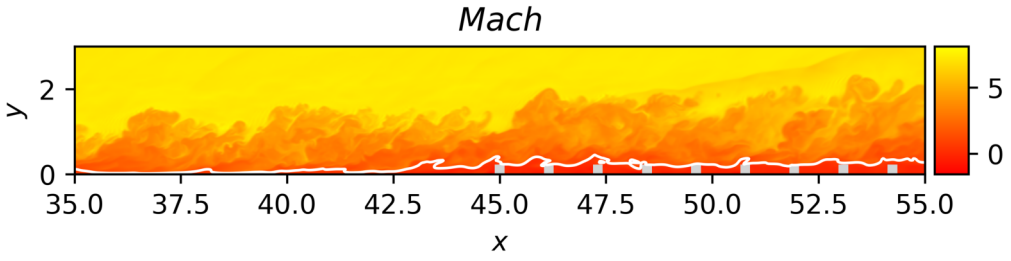

(c) $k^+ = 30$

Figure 12: Wall-normal slice of instantaneous mach number field

Clearly the only regions characterized by a subsonic flow are inside the boundary layer. The flow satisfies the no-slip condition, which means that the velocity at the wall is zero.
In the smooth case the flow almost immediately recovers its hypersonic nature, because it is not slowed down by the roughness elements. As a consequence the subsonic area is very thin and almost completely attached to the wall.
In the rough cases, on the contrary, the flow behaves differently. For $k^+ = 15$ there is a bigger subsonic region directly before and above the first roughness element. That is the area behind the shock wave, where the fluid underwent a compression wave and the flow is subsonic .
For $k^+ = 30$ the subsonic area is even bigger. As explained before, the whole region between the roughness elements is characterized by very low velocity.

6.1.4 Instantaneous density field

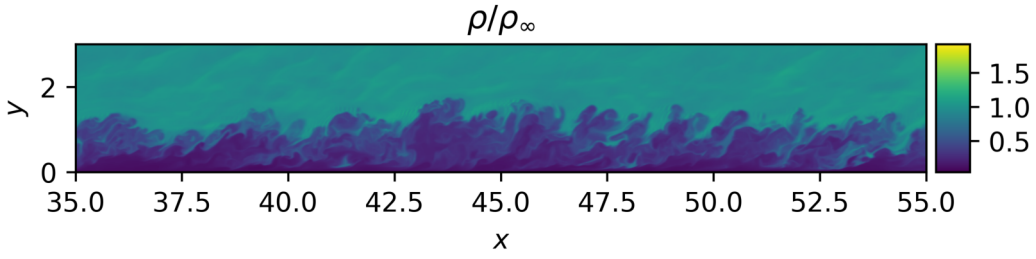

(a) $k^+ = 0$

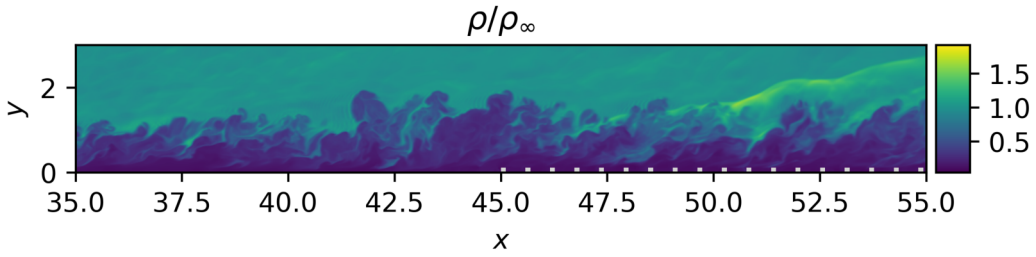

(b) $k^+ = 15$

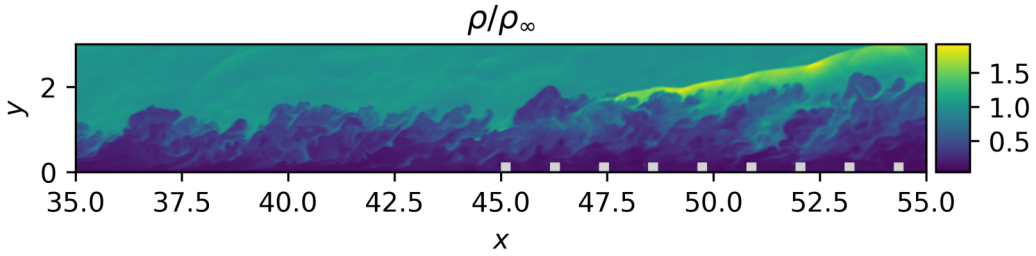

(c) $k^+ = 30$

Figure 13: Wall-normal slice of instantaneous field of density

The analysis of the density of the fluid is the one that better shows the presence of the shock wave. From Figure 13 it is clearly visible how the density reaches very high values in correspondence with the shock wave line. It is visible in both the rough cases. The shock wave in the case with $k^+ = 30$ is more intense.
The shock wave is caused not only by the presence of the roughness element, but also by its effect on the boundary layer: the boundary layer thickness increases in correspondence with the roughness elements, and as a consequence the incoming flow detects a mass of fluid with low velocity that in this case acts as a body that interacts with the flow and creates the conditions for the creations of the shock wave.

6.1.5 Mean density field

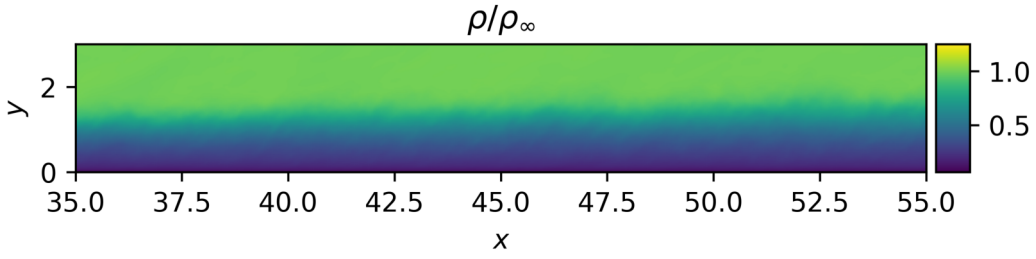

(a) $k^+ = 0$

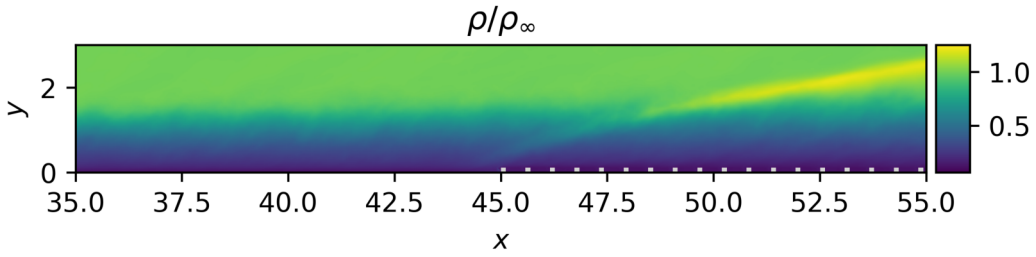

(b) $k^+ = 15$

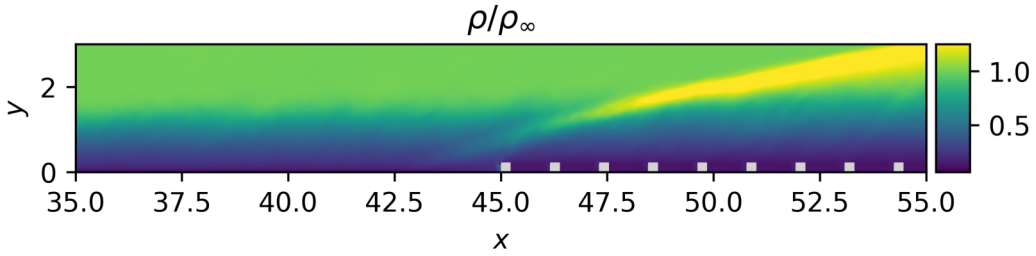

(c) $k^+ = 30$

Figure 14: Wall-normal slice of mean field of density

14

The mean density field shown in Figure 14 is useful for a better analysis of the shock wave and of the boundary layer thickness.
The mean density filed in the smooth case is completely uniform, it doesn't present any particular feature because the flow is not disturbed by anything. One important aspect to take into account, however, is the boundary layer height δ, that can be compared with the two rough cases.
In images b and c of Figure 14 it's immediately visible the presence of the shock wave. By comparing the two cases, we can clearly see how the shock gains intensity as the roughness height increases; in fact, the area occupied by the shock in the second case is wider and characterized by higher values of density. By comparing the two rough cases we can see that the second is characterized by a higher angle, and that can be explained by the fact that the roughness elements are higher; as a consequence the boundary layer thickness is bigger, and these two aspects together cause the flow to interact with a bigger stationary mass. The bigger is the object, the bigger will be the angle of the shock wave that said object causes.

6.2 Wall-parallel plane

In these paragraphs the wall-parallel slices of the velocity and temperature fields will be examined. Each picture will show the field in exam on three different levels in order to analyse the behaviour of the flow as we gradually move up away from the wall. The distance from the wall is rendered adimensional by dividing the coordinate y with the value of δ_{99} calculated at station $x = 40\delta_{in}$, where boundary layer is not influenced by the presence of the boundary elements yet.

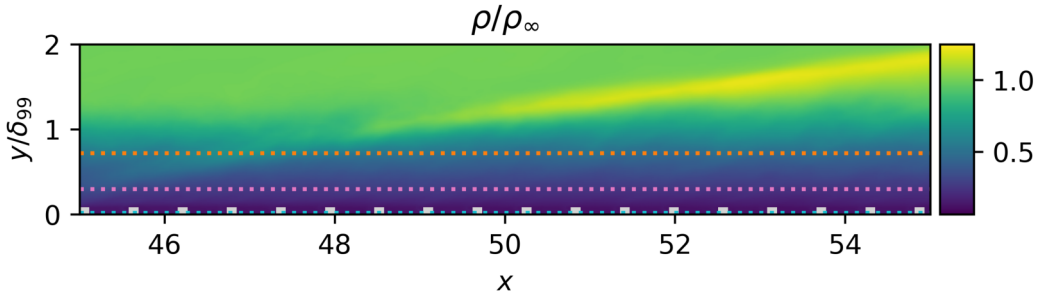

(a)

Figure 15: Wall-normal slice of the mean density field for the case with $k^+ = 30$. The three lines represent three boundary layer levels. Starting from the wall and moving upwards, the first includes the roughness micro structure, the second is an intermediate zone, the third in on the edge of the boundary layer

The first level is at $y/\delta_{99} = 0.02$, which is the nearest to the wall of the three levels that will be considered. Because of this closeness to the wall but more importantly to the roughness elements, the micro structures of the fluid caused by the roughness itself are still visible. The second level is a little higher, placed at $y/\delta_{99} = 0.30$, enough to show that the flow is still influenced by the roughness elements, but the effect of the singular element is no longer visible and the flow is starting to recover the external flow. The last level is on the edge of the boundary layer, with $y/\delta_{99} = 0.72$, and the effects of the roughness elements are still visible in some cases but the flow has almost completely recovered the external flow.

6.2.1 Instantaneous velocity field

The next three paragraphs are dedicated to the analysis of the velocity field and its behaviour along the y direction.

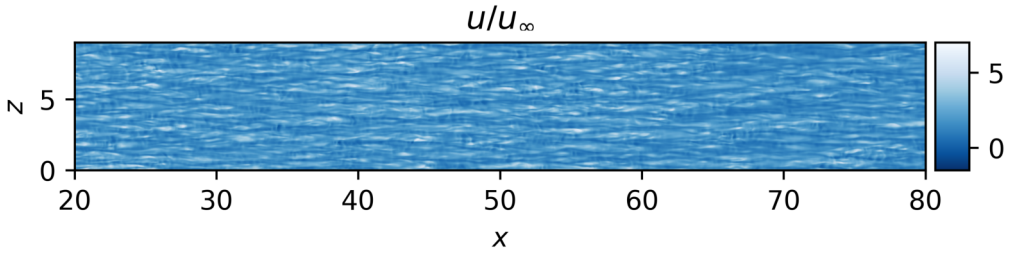

(a) $k^+ = 0$

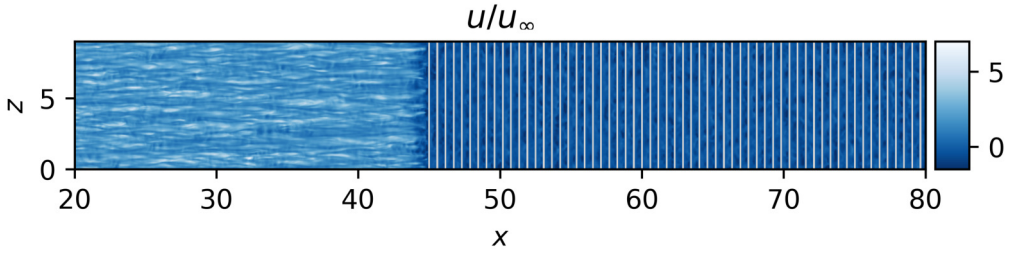

(b) $k^+ = 15$

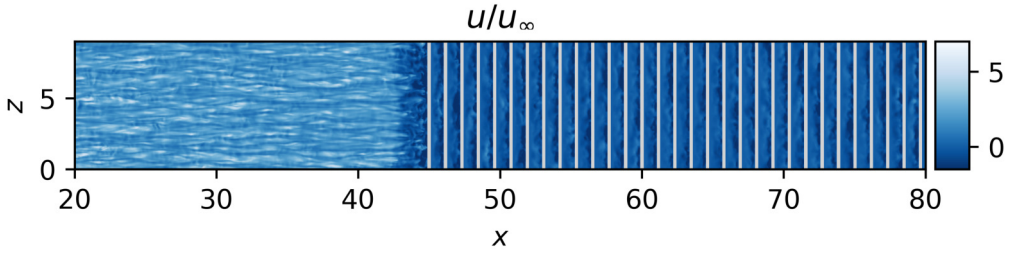

(c) $k^+ = 30$

Figure 16: Wall-parallel slice of instantaneous field of velocity at $y/\delta_{99} = 0.02$

As previously mentioned, this first layer is in close proximity of the wall and the roughness elements. As a consequence the velocities are relatively low.
At first sight one can immediately appreciate the difference between the the first half of the plate and the second half, where the roughness bars are present. In the region with the roughness elements the velocities are lower and the flow is strongly influenced by the roughness. It can still be identified the area between the roughness elements, where the velocity reaches its lower values that are, in some points, negative. This is due to the fact that region between two bars is characterized by recirculation.
By looking at the diagram Figure 23((b)) we can see that for value of $y/\delta_{99} = 0.02$ the gap between the smooth solution is big, which means that the magnitude of the velocity for the two rough cases is significantly smaller than the magnitude of the velocity of the smooth case.

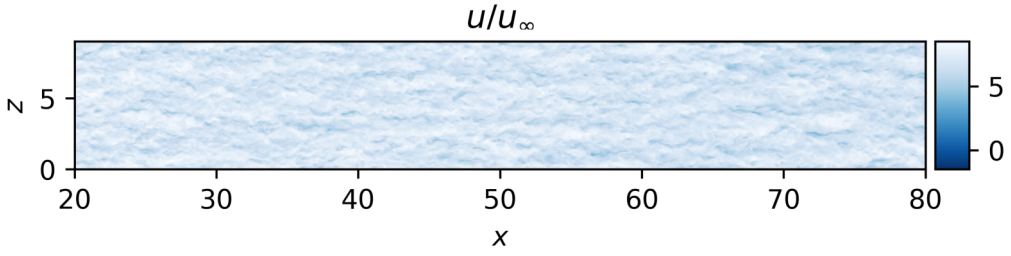

(a) $k^+ = 0$

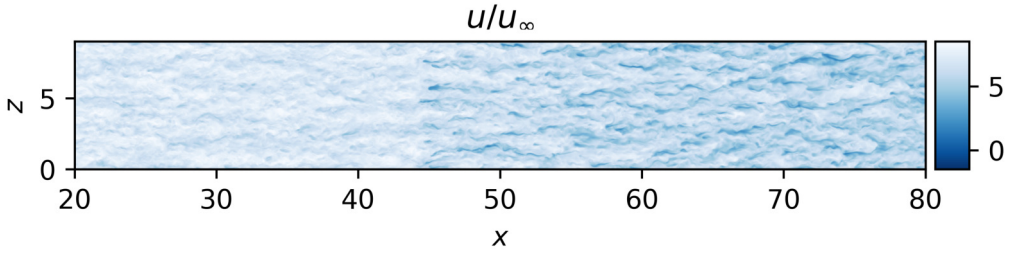

(b) $k^+ = 15$

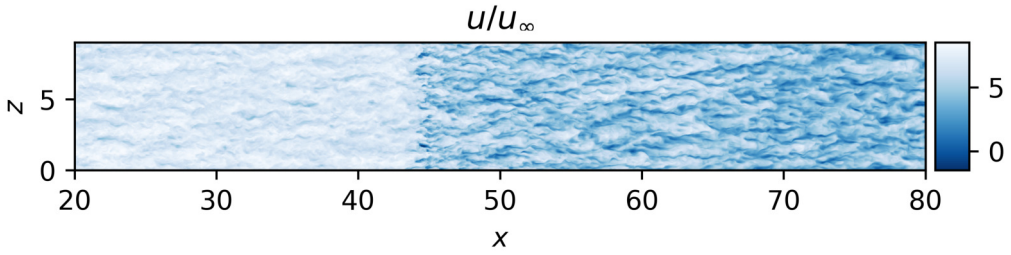

(c) $k^+ = 30$

Figure 17: Wall-parallel slice of instantaneous field of velocity at $y/\delta_{99} = 0.3$

In this case the distance from the wall is bigger and for this reason the region has lost some dependence from the roughness, but it's still well inside the boundary layer.
Overall the fluid is characterized by higher values of velocity, because this section is farther away from the wall and the flow is starting to recover the external solution. The effect of the roughness elements, however, is not negligible yet as the velocities of both the rough cases are slowed down . The difference with the previous case is that at this level we can not appreciate the effect of the single bar on the fluid and from the simple analysis of these images it is not possible to assume the shape of the roughness elements that generated this flow. As this works proceeds, more roughness shapes could be taken into account and the goal is to demonstrate that the final results are independent from the type of elements used, but are only influenced by their dimensions.
Like before, by comparing these results with Figure 23 ((b)) we can find a confirmation of the validity of these conclusions, because for $y/\delta_{99} = 0.30$ the smooth and rough solutions are still distant from one another, but the gap is smaller, which means that they are both leaning towards the same solution.
The last and higher level is on the edge of the boundary layer, where the effects of the roughness have little influence because we are closer to the outer flow. It can be seen in both the rough

cases have, and in particular in the rough case with $k^+ = 15$ the flow has almost completely recovered the external solution.
This finds confirmation in Figure 23 ((b)), where for the value of $y/\delta_{99} = 0.72$ the curves of the smooth and rough solutions are almost coincident, because, as explained before, this section is on the edge of the boundary layer, and that means that the solution has almost completely recovered the external solution

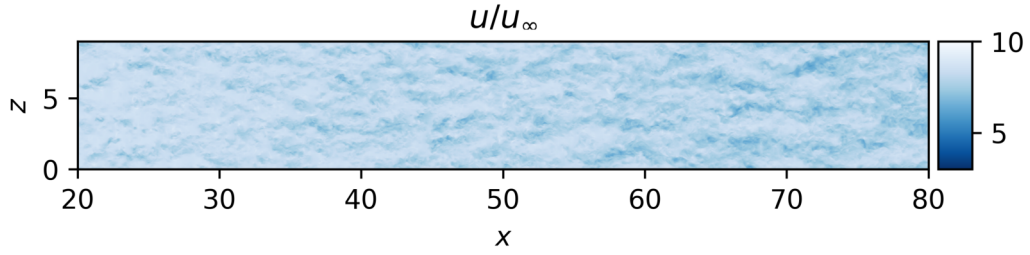

(a) $k^+ = 0$

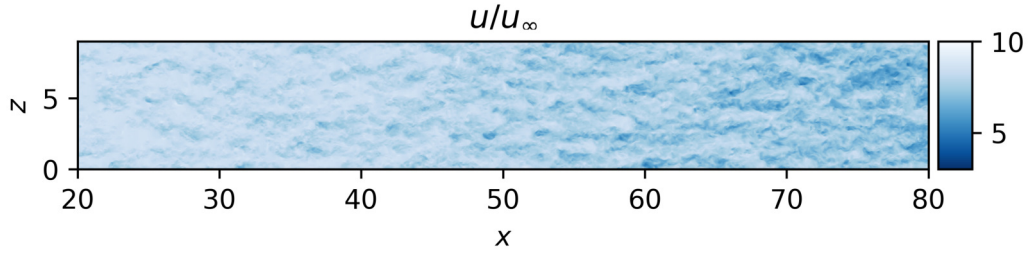

(b) $k^+ = 15$

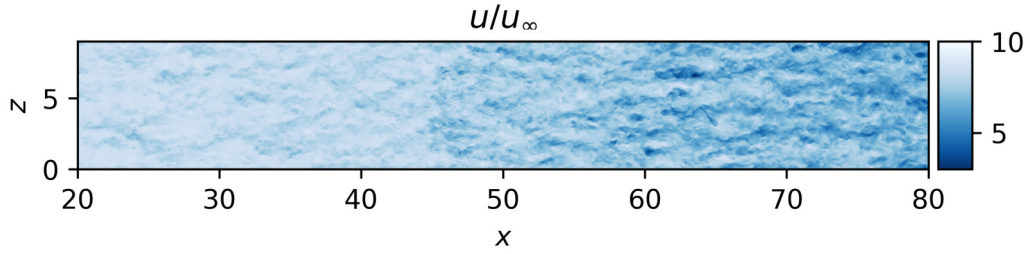

(c) $k^+ = 30$

Figure 18: Wall-parallel slice of instantaneous field of velocity at y/$\delta_{99} = 0.72$

6.2.2 Instantaneous temperature field

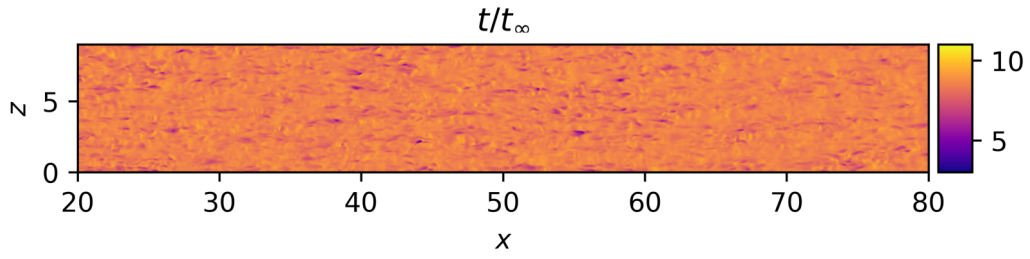

(a) $k^+ = 0$

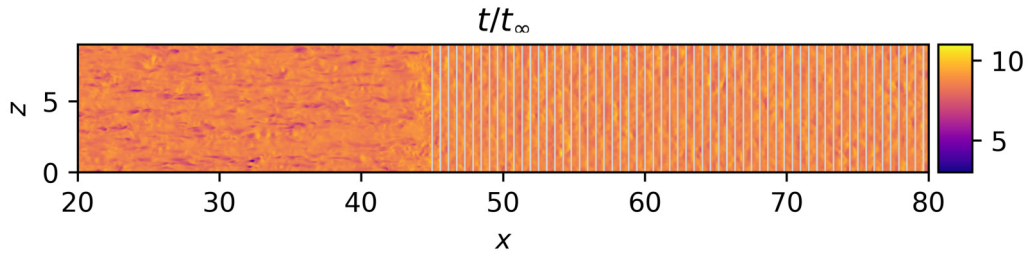

(b) $k^+ = 15$

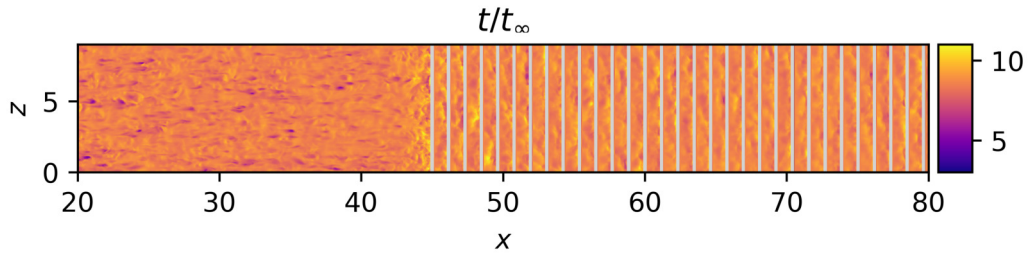

(c) $k^+ = 30$

Figure 19: Wall-parallel slice of instantaneous field of temperature at $y/\delta_{99} = 0.02$

The temperature is visibly high in the whole plate, because at this distance from the wall the viscous effects are stronger and they create heat that increases the temperature of the flow. In the case with $k^+ = 30$ there are some hot spots that greatly increase the wall heat.
The area between the bars is characterized by higher values of temperature, because the roughness causes Similarly to the velocity, the temperature field at this height level still has the shape of the bars and the flow is influenced by the microstructure of the roughness elements.

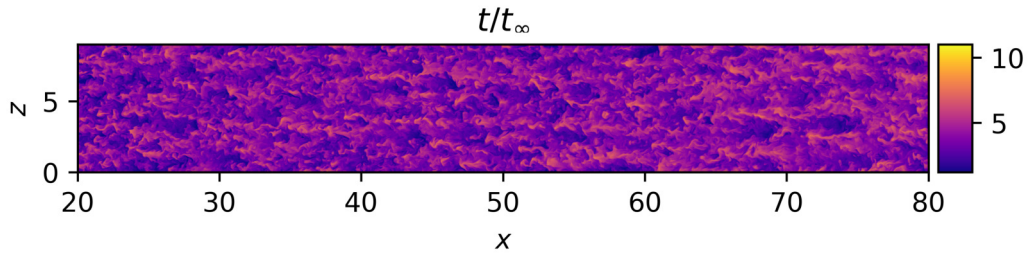

(a) $k^+ = 0$

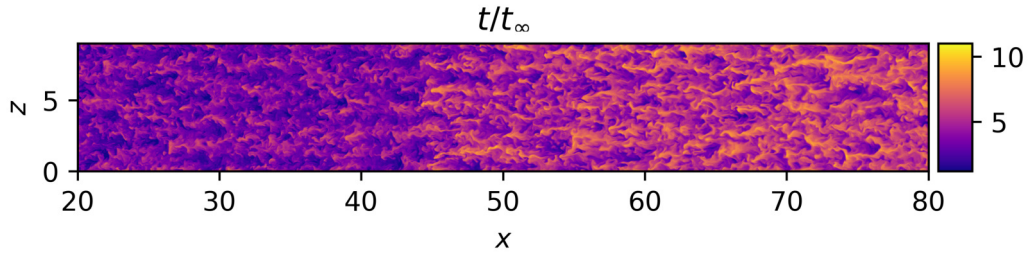

(b) $k^+ = 15$

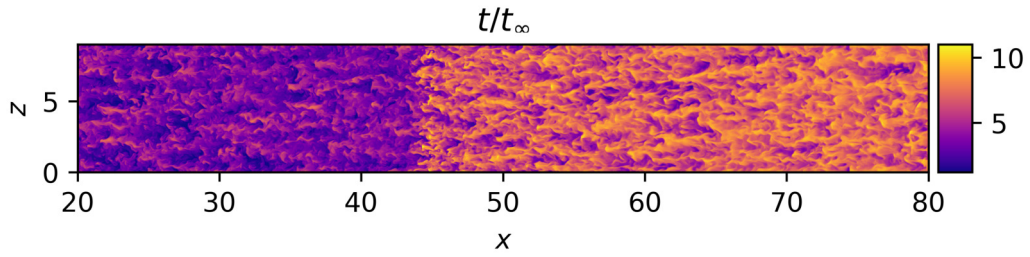

(c) $k^+ = 30$

Figure 20: Wall-parallel slice of instantaneous field of temperature at y/δ_{99} = 0.3

Moving away from the wall in the y direction the flow loses its dependence from the shape of the roughness and is uniform in the structures. In this case the difference between the temperature in the first portion of the plate and the temperature in the portion occupied by the roughness elements is bigger than the previous case at $y/\delta_{99} = 0.02$, and this finds confirmation in the monodimensional profile at Figure 23((c)). It can be seen how in the first portion of the plot the temperatures has the same value for all the three cases, and at some point the curves of the rough cases start to differ from the smooth case, until they converge again at values of y/δ_{99} equal to about 0.75. At this level the effects of the roughness start to become negligible. As shown before the velocity field is no longer influenced by the bars, and the same happens with the temperature field: in the last section that we analyze, that corresponds to $y/\delta_{99} = 0.72$, Figure 21, the fluid's temperature is only slightly bigger in the second rough cases than in the smooth case, while in the first rough cases the difference in barely visible, because the boundary layer's thickness is smaller and at this level the flow is on the edge of the boundary layer.

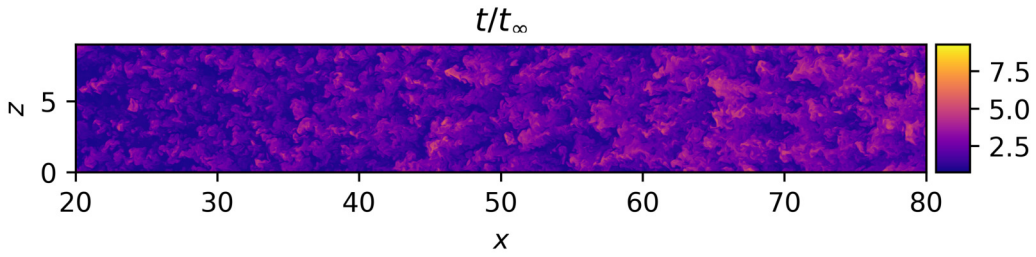

(a) $k^+ = 0$

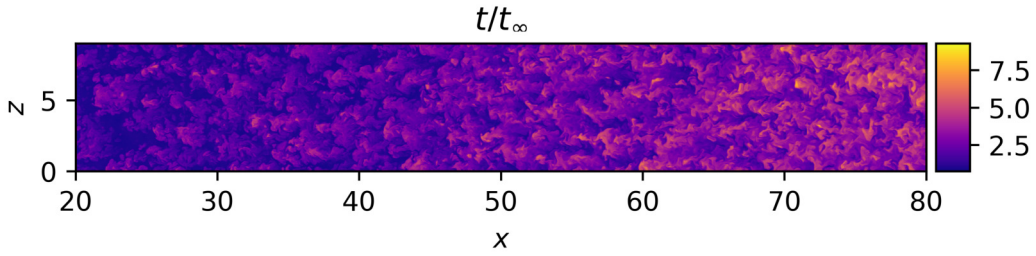

(b) $k^+ = 15$

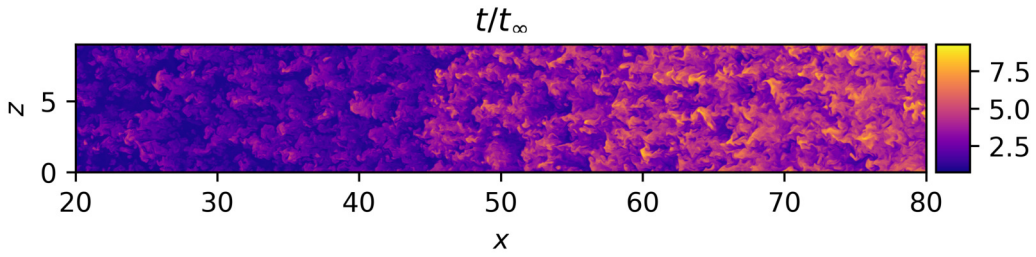

(c) $k^+ = 30$

Figure 21: Wall-parallel slice of instantaneous field of temperature at $y/\delta_{99} = 0.72$

6.3 Averaged and root mean square statistics

The following images show the mean profiles of the boundary layer thickness δ_{99} and of the adimensional variables temperature, velocity, and root mean square temperature along the y direction for each case, calculated in correspondence with the reference station $x = 70\delta_{in}$.

While calculating the mean values of the variables there was the problem that the values at the stations in correspondence to the bar elements where different than the ones at the level of the "valley" between them, and in particular inside the bars there is no fluid, so there are no values at all. For this reason the average process takes into consideration the presence of the roughness elements by calculating two different mean values in the around of the considered station ($x = 70\delta_{in}$), the first is an half period before $x = 70\delta_{in}$, in correspondence with a bar element, the second is a half period after the considered station, inside the valley. While y is bigger than the roughness height the two averages coexist and they blend in the average process; when y is smaller the value of the average discontinuously becomes the value of the valley alone.

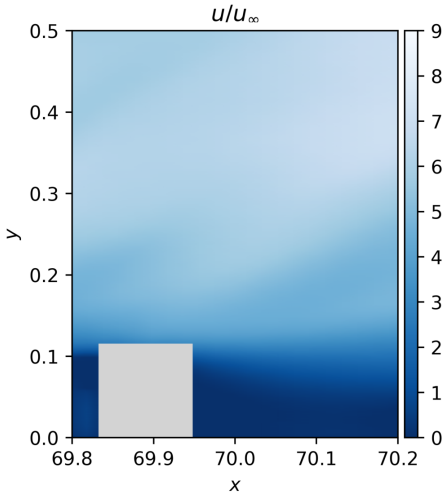

Figure 22: Zoom in of the reference station's proximity

In proximity with the rough elements the difference between the two behaviours will be significant, but as we move away from the wall they will be more and more similar until they will no longer differ. As will be clear from the one dimensional profiles, this study shows that we can identify three main regions based on the flow's behaviour. The region closest to the wall is strongly influenced by the roughness and the two different behaviours (valley and peak) are still visible; at the edge of the boundary layer the flow does not sense the presence of the roughness if not for the fact that the boundary layer's height increases; the area between these two region is still influenced by the bar elements, but the microstructure of the roughness is no longer visible and the flow is homogeneous.

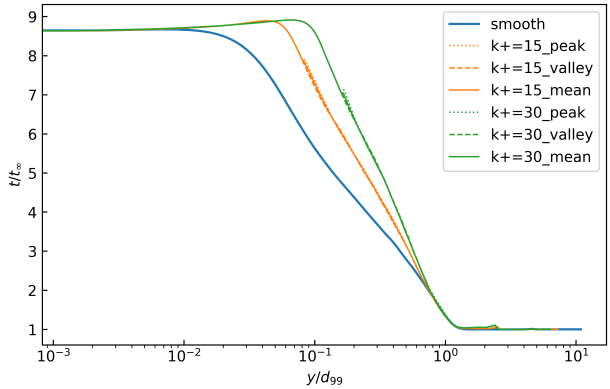

(a) Mean temperature profile as function of y/δ_{99} for each case

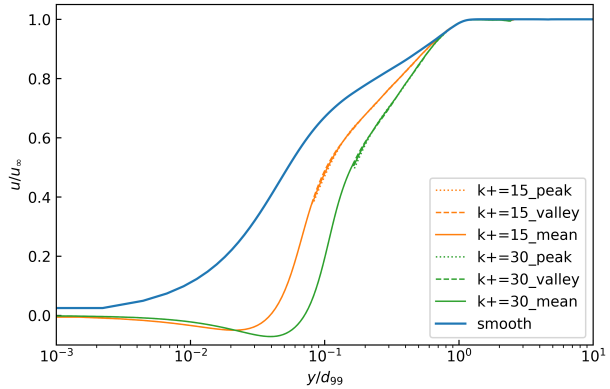

(b) Mean velocity profile as function of y/δ_{99} for each case

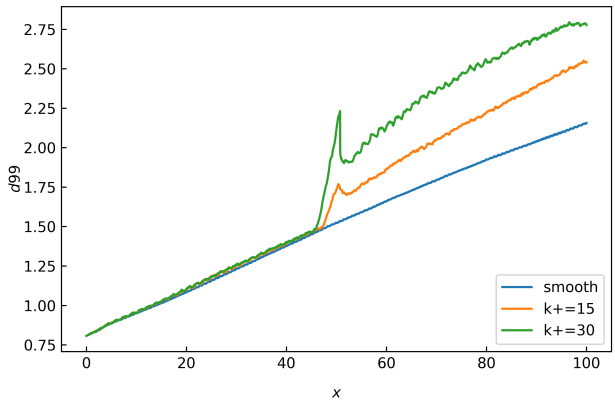

(c) Boundary layer thickness (δ_{99}) for each case

Figure 23: Mean statistics where x=70δ_{in} is the reference station

This one dimensional profile of the temperature, rendered adimensional with the temperature of the outer flow, is a confirmation of what was said before. The higher values of temperature can be found in the region closest to the wall, where the flow is slowed down because of the effect of friction, which creates heat that causes the fluid's temperature to increase. Further from the wall the temperature gradually decreases and until it recovers the external value outside the boundary layer, where the viscous effects are negligible. For the two rough cases the dotted lines represents the two averages for peak and valley of the bars, and the continuous line is the mean value of the two, as explained before. For values of y/δ_{99} close to the roughness height these lines differ, but as we move long the y direction they start to be indistinguishable from one another. Furthermore, in correspondence with the peak of the bar element the mean value discontinuously becomes the value of the valley average alone.

The velocity profile of the smooth case allows us to observe the behaviour inside the boundary layer and how it respects the law of the wall explained in the first chapter. If the plot was in internal coordinates, the first portion of the profile would follow the linear law and the last portion of the boundary layer would follow the logarithmic law; the area between these two regions is the buffer layer, where the velocity doesn't follow any of the two previously mentioned laws.
The roughness causes a flow retardation throughout the profile. Close to the wall, the mixing due to the roughness elements causes the flow to become more uniform in velocity, especially

for the larger roughness elements. These results are in parallel with the results in [19]. We can compare the plots and observe that the velocity profiles have the same behaviours.
The values of the velocities in the two rough cases differ from the value of the smooth cases of a considerable amount in the proximity of the roughness, because the flow is slowed down as the energy of the incoming flow is converted in heat. The higher are the roughness elements, the more the velocity profile moves away from the smooth case, as we can see in Figure 23 (b), where the green line represents the second rough case with higher bars, and its velocity profile is shifted right and down. Another important aspect that can be seen is that the velocity in the two rough cases reaches negative values near the wall, because of the recirculation that happens between the bars. Similarly to the temperature, the profiles of the rough cases are the mean values of the two cases, peak and valley.
For values of y/δ_{99} close to 0.75 the velocities of the three cases are almost overlying, which demonstrate that a big portion of the boundary layer, more or less 25%, is not influenced by the presence of the roughness, since the flow has recovered the behaviour of the smooth case.

The analysis of δ_{99} clearly shows the presence of the initial shock wave and the effect that the roughness has on the boundary layer thickness itself. Right before the first element the value of δ_{99} increases abruptly forming a peak in the profile, reaching higher values in the second rough case. After this sudden increase, the boundary layer thickness keeps growing in a more regular way, following the development of the smooth case but shifted upwards of a certain amount that depends on the roughness thickness.

6.3.1 Velocity and temperature fluctuations

In the next paragraphs, the analysis is made for the Root Mean Square (RMS) fields, which show the mean intensity of the fluctuations in specific point of the domain and is obtained as the square root of the mean of the squares of the values set.

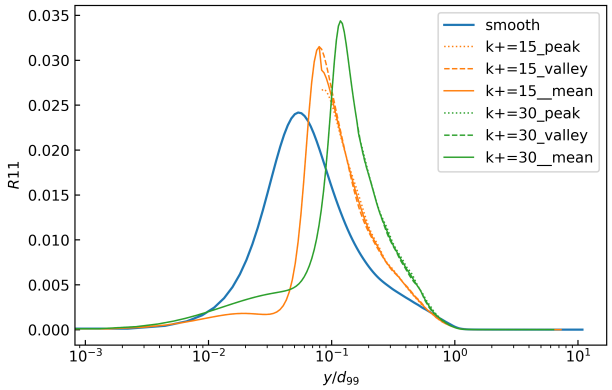

(a) Streamwise component of velocity stress tensor

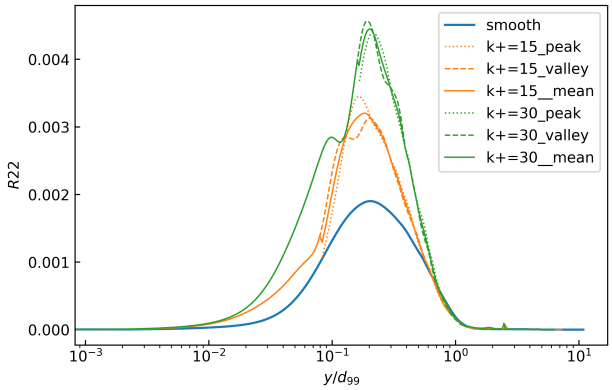

(b) Wall-normal component of velocity stress tensor

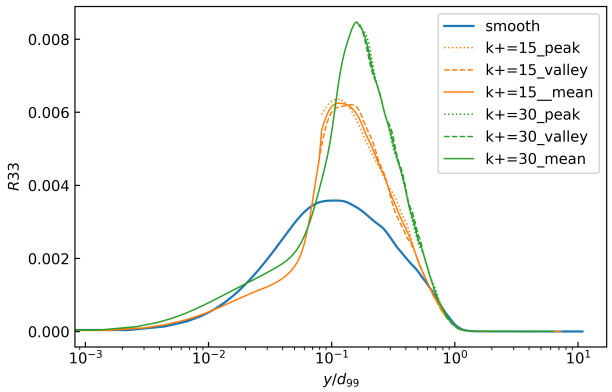

(c) Spanwise component of velocity stress tensor

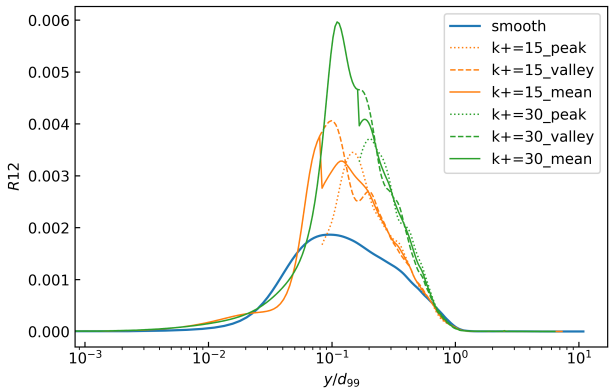

(d) Reynolds stress

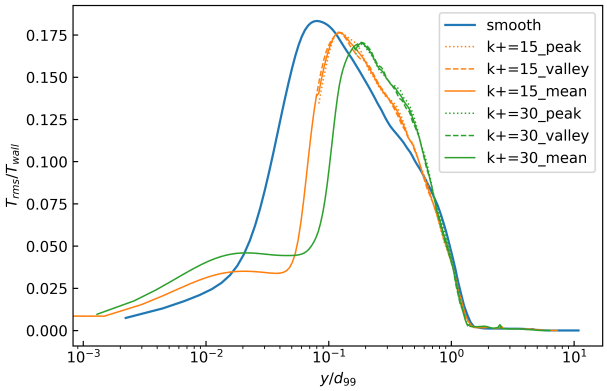

(e) Mean root mean square of temperature profile for each case

Figure 24: Velocity fluctuations for each case

As one could imagine, the velocity fluctuations increase when roughness is present, as it triggers the boundary layer and makes it turbulent, causing the fluctuating terms of the velocity to

become bigger and not negligible. In all the cases in exam the fluctuations are concentrated around the roughness elements, where the flow is the most turbulent
The components of the velocity fluctuations along the streamwise direction, Figure 24 (a), are the ones that undergo less changes, as the peak reaches higher values but the difference with the smooth case is smaller compared with the increase of the other fluctuation components. Another difference is the fact that this is the only case in which the peak is shifted not only upwards but also towards the right of the graphic, something that doesn't happen in the other cases. In the plot of the mixed components,Figure 24 (d), one can notice that the peak and valley averages differ from one another of a considerable amount, as opposed to the other graphics where the difference is much smaller.

7 Conclusions

We conducted tree Direct Numerical Simulations (DNS) of an hypersonic flow over a flat plate with different levels of roughness. In the first case the surface of the plate is smooth, in the other two cases roughness a series of square bars elements, with different dimensions for the two cases, are placed on the plate along the streamwise direction. The results of the two roughness cases have been compared with the smooth one in order to appreciate the effect of roughness on a series of variables such as velocity, density, temperature and boundary layer thickness.

Three main levels along the y direction were identified, based on the flow behaviour with respect to the presence of roughness. The first one, closest to the wall but more importantly to the roughness elements, is characterized by the fact that the flow is still strongly influenced by the micro-structure of the roughness geometry and the stagnant fluid in the areas between the bars increases as the roughness height increases. The second level is placed at $y/\delta_{99} = 0.30$, which corresponds to a transition area, relatively far from the wall, where the flow is still influenced by the roughness elements, but the effect of the singular element is no longer visible, the flow is more uniform and it is starting to recover the external flow. The last level is on the edge of the boundary layer, with $y/\delta_{99} = 0.72$, and the effects of the roughness elements are still visible in some cases but the flow has almost completely recovered the smooth solution that follows Townsend hypothesis.

The results have been compared with Williams et al. [19]: it can be seen how in both studies we see a strong flow retardation due to roughness throughout the profile, effect that increases with the roughness height k. The mean velocity profiles are shifted downward as a consequence of the presence of roughness enhanced mixing due to the roughness elements causes the flow to become more uniform in velocity, especially for the larger roughness elements. So, the results of this simulation are conformed with the experimental results, in the limits of this analysis, the main difficulty of which have been the lack of the wall shear stress τ_w as a function of x, necessary to compute the wall parameters such as Re_τ or u_τ.

The shear stress τ_w is not only given by the viscous component $\mu\frac{\partial u}{\partial y}$, but also by the pressure drag that comes from the pressure forces on the rough elements faces, which makes its computation more difficult. The knowledge of the value of the shear stress in the study of turbulent boundary layers is fundamental, and for this reason it is the main goal for future works, in order to obtain a thorough analysis of compressible flows as it has been already done for incompressible flows.

References

[1] Bernardini, Matteo et al. "STREAmS: a high-fidelity accelerated solver for direct numerical simulation of compressible turbulent flows". In: *Computer Physics Communications* 263 (2021), p. 107906.

[2] Chung, Daniel et al. "Predicting the drag of rough surfaces". In: *Annual Review of Fluid Mechanics* 53 (2021).

[3] De Vanna, Francesco. "A high-resolution fully compressible Navier-Stokes solver for analysis of moving objects at high Mach numbers". PhD thesis. Università degli Studi di Padova, 2018.

[4] Flack, Karen A and Schultz, Michael P. "Roughness effects on wall-bounded turbulent flows". In: *Physics of Fluids* 26.10 (2014), p. 101305.

[5] Hatcher, Allen. *Algebraic topology.*, 2005.

[6] Jiménez, Javier. "Turbulent flows over rough walls". In: *Annu. Rev. Fluid Mech.* 36 (2004).

[7] Kocher, Brian D et al. "Characterizing the streamwise development of surface roughness effects on a supersonic boundary layer". In: *2018 Fluid Dynamics Conference*. 2018, p. 4047.

[8] Latin, Robert M and Bowersox, Rodney DW. "Flow properties of a supersonic turbulent boundary layer with wall roughness". In: *AIAA journal* 38.10 (2000), pp. 1804–1821.

[9] Mittal, Rajat and Iaccarino, Gianluca. "Immersed boundary methods". In: *Annu. Rev. Fluid Mech.* 37 (2005).

[10] Modesti, Davide et al. "Direct numerical simulation of supersonic turbulent flows over rough surfaces". In: *Journal of Fluid Mechanics* 942 (2022).

[11] Moin, Parviz and Mahesh, Krishnan. "Direct numerical simulation: a tool in turbulence research". In: *Annual review of fluid mechanics* 30.1 (1998), pp. 539–578.

[12] Nikuradse, Johann et al. "Laws of flow in rough pipes". In: (1950).

[13] Peltier, SJ, Humble, RA, and Bowersox, RDW. "Crosshatch roughness distortions on a hypersonic turbulent boundary layer". In: *Physics of Fluids* 28.4 (2016), p. 045105.

[14] Pope, Stephen B and Pope, Stephen B. *Turbulent flows*. Cambridge university press, 2000.

[15] Townsend, AAR. *The structure of turbulent shear flow*. Cambridge university press, 1980.

[16] Van Driest, E Reginald. *The problem of aerodynamic heating*. Institute of the Aeronautical Sciences, 1956.

[17] Venkatapathy, E et al. "Thermal protection system development, testing, and qualification for atmospheric probes and sample return missions: Examples for Saturn, Titan and Stardust-type sample return". In: *Advances in Space Research* 44.1 (2009), pp. 138–150.

[18] Wilder, Michael C and Prabhu, Dinesh K. "Rough-wall turbulent heat transfer experiments in hypersonic free flight". In: *AIAA Aviation 2019 Forum*. 2019, p. 3009.

[19] Williams, Owen JH et al. "Effects of roughness on a turbulent boundary layer in hypersonic flow". In: *Experiments in Fluids* 62.9 (2021), pp. 1–13.

[20] Zhang, You-Sheng et al. "A generalized Reynolds analogy for compressible wall-bounded turbulent flows". In: *Journal of Fluid Mechanics* 739 (2014), pp. 392–420.